International Journal of Hyperthermia

ISSN: (Print) (Online) Journal homepage: https://www.tandfonline.com/loi/ihyt20

Computational modeling of microwave ablation with thermal accelerants

Jan Sebek, William K. C. Park, Shireen Geimer, Douglas W. Van Citters, Alexandra Farah, Damian E. Dupuy, Paul M. Meaney & Punit Prakash

To cite this article: Jan Sebek, William K. C. Park, Shireen Geimer, Douglas W. Van Citters, Alexandra Farah, Damian E. Dupuy, Paul M. Meaney & Punit Prakash (2023) Computational modeling of microwave ablation with thermal accelerants, International Journal of Hyperthermia, 40:1, 2255755, DOI: 10.1080/02656736.2023.2255755

To link to this article: https://doi.org/10.1080/02656736.2023.2255755

© 2023 The Author(s). Published with license by Taylor & Francis Group, LLC

Published online: 14 Sep 2023.

Submit your article to this journal

Article views: 408

View related articles

View Crossmark data

Full Terms & Conditions of access and use can be found at https://www.tandfonline.com/action/journalInformation?journalCode=ihyt20

INTERNATIONAL JOURNAL OF HYPERTHERMIA
2023, VOL. 40, NO. 1, 2255755
https://doi.org/10.1080/02656736.2023.2255755

Taylor & Francis
Taylor & Francis Group

OPEN ACCESS Check for updates

Computational modeling of microwave ablation with thermal accelerants

Jan Sebek[a], William K. C. Park[b], Shireen Geimer[c,d], Douglas W. Van Citters[d], Alexandra Farah[b], Damian E. Dupuy[b], Paul M. Meaney[d] and Punit Prakash[a]

[a]Department of Electrical and Computer Engineering, Kansas State University, Manhattan, Kansas, USA; [b]Theromics, Inc., West Bridgewater, Massachusetts, USA; [c]Expeditionary School at Black River, Ludlow, Vermont, USA; [d]Thayer School of Engineering, Dartmouth College, Hanover, New Hampshire, USA

ABSTRACT

Purpose: To develop a computational model of microwave ablation (MWA) with a thermal accelerant gel and apply the model toward interpreting experimental observations in *ex vivo* bovine and *in vivo* porcine liver.

Methods: A 3D coupled electromagnetic-heat transfer model was implemented to characterize thermal profiles within *ex vivo* bovine and *in vivo* porcine liver tissue during MWA with the HeatSYNC thermal accelerant. Measured temperature dependent dielectric and thermal properties of the HeatSYNC gel were applied within the model. Simulated extents of MWA zones and transient temperature profiles were compared against experimental measurements in *ex vivo* bovine liver. Model predictions of thermal profiles under *in vivo* conditions in porcine liver were used to analyze thermal ablations observed in prior experiments in porcine liver *in vivo*.

Results: Measured electrical conductivity of the HeatSYNC gel was ~83% higher compared to liver at room temperature, with positive linear temperature dependency, indicating increased microwave absorption within HeatSYNC gel compared to tissue. In *ex vivo* bovine liver, model predicted ablation zone extents of (31.5×36) mm with the HeatSYNC, compared to ($32.9 \pm 2.6 \times 40.2 \pm 2.3$) mm in experiments (volume differences $4 \pm 4.1\ cm^3$). Computational models under *in vivo* conditions in porcine liver suggest approximating the HeatSYNC gel spreading within liver tissue during ablations as a plausible explanation for larger ablation zones observed in prior *in vivo* studies.

Conclusion: Computational models of MWA with thermal accelerants provide insight into the impact of accelerant on MWA, and with further development, could predict ablations with a variety of gel injection sites.

ARTICLE HISTORY
Received 30 March 2023
Revised 30 August 2023
Accepted 31 August 2023

KEYWORDS
Thermal accelerant; microwave ablation; tumor ablation

Introduction

Image-guided thermal ablation (IGTA) of tumors has been used clinically for the treatment of focal tumors in the liver, lung, kidney, and bone [1–5]. While IGTA can be performed as a standalone therapy, more recently the procedure has been combined with chemotherapy or radiotherapy [6,7]. Minimally invasive IGTA procedure offers several advantages over traditional surgical resection, which include lower morbidity, improved preservation of surrounding tissue, and a reduction in hospitalization costs and length of stay [8]. Technology development and clinical studies of thermal ablation were initially performed with radiofrequency (RF) energy-based systems operating at frequencies in the range ~350 – 500 kHz. While RF ablation remains the most widely-used platform available in clinical use worldwide, it suffers from several significant limitations: relatively long treatment times, limited penetration, difficulties in creating uniform ablation zones of tissue, and biophysical tissue interactions that ultimately limit RF heating including tissue charring and vaporization [1]. Microwave (MW – commonly referring to frequencies between 915 MHz and 2.45 GHz, although higher frequency systems have also been explored) ablation platforms have been developed and investigated [9,10], and offer advantages including the ability to achieve higher temperatures (> 100 °C) with larger ablation zones in less time. MW is less vulnerable to blood flow-induced heat sink effects [10–12] and to impedance-driven performance variability compared to RF ablation. Commercial microwave ablation (MWA) platforms have become available [13] with initial clinical studies demonstrating their safety and efficacy [9,14–17]. MWA systems are increasingly used in the clinical setting, with several new MWA systems currently under development [18,19].

Despite these technological improvements, reliably achieving large-volume heating (> 2–3.5 cm) during clinical MWA procedures remains a challenge [20,21]. To overcome this challenge, one approach is to apply simultaneous ablation with multiple antennas [22] or single antenna serial applications [21,23]. However, general use may be limited by

CONTACT Punit Prakash prakashp@ksu.edu Department of Electrical and Computer Engineering, Kansas State University, 3078 Engineering Hall, 1701D Platt St, Manhattan, KS 66506, USA.

© 2023 The Author(s). Published with license by Taylor & Francis Group, LLC
This is an Open Access article distributed under the terms of the Creative Commons Attribution License (http://creativecommons.org/licenses/by/4.0/), which permits unrestricted use, distribution, and reproduction in any medium, provided the original work is properly cited. The terms on which this article has been published allow the posting of the Accepted Manuscript in a repository by the author(s) or with their consent.

anatomical difficulties in antenna placement and inconsistent ablation results due to varying energy penetration, tumor tissue differences and collateral tissue injuries, e.g., to the bile duct, nerves, and gall bladder [24].

While temperatures near the MW antenna can exceed 110 °C during ablation, tissue thermal conductivity is generally low such that steep temperature gradients are observed which limit the radial penetration of the ablation zone outwards from the applicator [25]. The goal of an ablation procedure is to extend the ablation zone over the tumor and a surrounding margin of normal tissue (referred to as a treatment margin). Biophysical factors that contribute to the relatively high local recurrence rate (>30%) are the heat sink effect and insufficient energy penetration [26]. The former is likely due to heat loss rendered by rapid blood flow through large blood vessels adjacent to the ablation site. The latter is primarily due to the attenuation of electromagnetic energy radiated by the antenna and low thermal conductivity of tissue leading to the creation of a narrow elliptical heating pattern along the antenna shaft, resulting in a shorter ablation reach in the transverse plane. Over the past two decades, attempts to overcome these barriers and increase the ablated volume have been made with modest success [20]. These include (a) introduction of saline solutions into the heating zones which resulted in burns along the least resistant channel through which the hot vapor could escape [27] and (b) insertion of additional antennas into adjacent spaces for broader ablation coverage, which is challenging from a safety perspective and can cause collateral injury to adjacent organs and other non-target tissues such as the bile ducts, ureters, and nerves [28].

To mitigate these challenges and improve treatment outcomes we have developed a thermal accelerant (TA) that aims to increase the ablation volume by more effective local absorption of the electromagnetic energy (microwave and radiofrequency energies). The thermal accelerant is a honey-like viscous fluid, with a viscosity of approximately 7,000 cP at room temperature. Molecules with higher dipole moments (e.g., NaCl, CsCl) were initially evaluated. Although these demonstrated some improvement in ablation performance, technical limitations and safety concerns outweighed the benefits [29,30]. Bovine serum albumin (BSA) is a large, biocompatible polymer protein with a favorably high dipole moment. However, by themselves even highly concentrated solutions of BSA did not produce the expanded temperature profiles desired during electromagnetic exposure because of strong internal protein-protein interactions [31]. To relieve these reciprocal actions and allow each albumin molecule to freely respond to the microwave energy, a chaotropic agent was introduced (e.g., NaCl); chaotropic agents are molecules in aqueous solution that can disrupt the network of hydrogen bonds between water molecules, weakening the hydrophobic effect, and thereby impacting the stability of the native state of macromolecules in solution. The BSA-based TAs with chaotropic agent demonstrated approximately fifty times greater thermal efficiency than ablation without the TA during the initial temperature rate increase and also augmented MW energy deposition more efficiently at larger distances from the antenna feed point (> 1.5 cm) to produce a larger ablation volume.

Based on these successful results in an animal model, a human TA formulation (e.g., HeatSYNC^{TM} gel [32]) was designed to have similar physical properties to the albumin counterpart. In prior *in vivo* animal studies, we demonstrated that ablation with the HeatSYNC gel produced a larger ablation volume and a more spherical shape than that of ablations without the gel in all tissues examined (e.g., liver, lung, muscle and kidney) under clinically-relevant MWA conditions [32–34]. When using a 915 MHz microwave ablation antenna powered with 60 W for 10 min together with the HeatSYNC gel, ablation zones were $6.80 \pm 0.62\,cm^3$ and $4.3 \pm 2.1\,cm^3$, respectively, in porcine liver and lung *in vivo*, compared to $2.69 \pm 0.36\,cm^3$ and $2.1 \pm 1.5\,cm^3$ without the HeatSYNC gel. Using a 2.45 GHz antenna powered at 100 W for 10 min with the HeatSYNC gel yielded ablation zones of volume $41.9 \pm 4.2\,cm^3$ in porcine muscle tissue *in vivo* compared to $28.7\,cm^3$ without the HeatSYNC gel. Example ablation zones achieved in porcine liver *in vivo* when using the HeatSYNC gel, and corresponding ablation zones in the absence of the gel, are illustrated in Figure 1. Application of the highly absorbing HeatSYNC gel at suitable locations from the MW applicator may also provide a means to serve as a thermoprotective agent. More sophisticated asymmetric tissue sculpting may be feasible when directional microwave antennas or multiple omnidirectional antennas with phase focusing are used with the HeatSYNC gel [19].

Computational models of microwave ablation have played an important role in the development of new ablation devices [35–39], comparative assessment of energy-delivery strategies [40], assessing the impact of heterogeneity in tissue properties on ablation profiles[41,42], and have contributed toward developing an understanding of the factors that influence the transient evolution of microwave ablation zones [43]. These models are also under investigation as part of treatment planning platforms that may serve as a clinical decision support tool to guide selection of treatment parameters on a patient-specific basis [44]. Advances in modeling of MW ablation procedures have benefited from detailed characterization of the electrical and thermal properties of tissue over the microwave frequency range, including dynamic changes as a function of temperature [45–48]. For the purposes of developing computational models of microwave absorption and thermal profiles in tissue during thermal ablation experiments involving the HeatSYNC gel, it is necessary to accurately know both the electrical and thermal properties of the materials for use in bioheat transfer models.

The present study was undertaken to develop a computational model for predicting ablation zone profiles during microwave ablation with the HeatSYNC gel. The model incorporates experimental measurements of the temperature-dependent dielectric and thermal properties of the HeatSYNC gel. Model predictions of transient temperature profile and ablation zone extents are compared against experiments conducted in fresh *ex vivo* bovine tissue. Finally, the model is employed to assess ablation zones under *in vivo* conditions in attempt to understand experimental observations from prior studies in porcine liver *in vivo*.

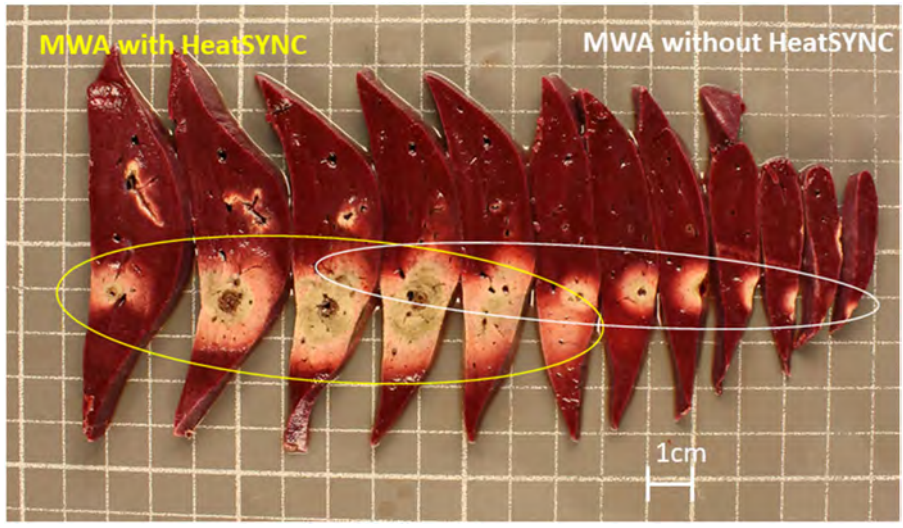

Figure 1. Example ablation zones in porcine liver *in vivo* following 60 W, 10 min MWA with a clinical ablation system (Perseon MicrothermX) when ablation was performed with (left) vs. without (right) ~2 ml HeatSYNC gel. The illustrated tissue sections are taken approximately perpendicular to the axis of the MWA applicator and were stained with TTC viability stain. The grid markings in the figure represent a distance of 1 cm.

Materials and methods

Measurement of dielectric and thermal properties of the HeatSYNC gel

The electrical properties (relative permittivity and electrical conductivity) help determine the actual microwave power absorption within a material. The dielectric properties, density, thermal conductivity and specific heat are necessary to accurately model the power absorption and conduction away from the heat source, and transient temperature profiles. One important complication in this process is that these properties are not constant as a function of temperature. To produce the most accurate model of the heating patterns, it is critical to know these properties as a function of temperature. For these experiments, published properties of liver tissue as a function of temperature are already available [45,46,49]. However, these properties are not known for the HeatSYNC gel. For this we performed a series of experiments to measure the dielectric properties, density, thermal conductivity and specific heat capacity of the HeatSYNC gel at temperatures over the range 20 – 90 °C.

For the dielectric properties and density, the measurements were performed in a controlled temperature bath (Isotemp 2150, Fisher Scientific, Waltham, MA) where the bath was allowed to equilibrate for a series of temperatures from 20 °C to 90 °C in 10 °C increments for 20 min at each temperature. Dielectric properties were measured with an 85070B dielectric probe kit and E5071B vector network analyzer (both from Agilent, Santa Rosa, CA). Following calibration of the probe with measurements on an open circuit, closed circuit, and deionized water, measurements on samples with known dielectric properties (ethanol, methanol) at room temperature were conducted. Density was determined from mass measurements performed with a Mettler Toledo XS105 mass scale (Columbus, OH) and volume measurements using a polystyrene 1 ml pipette (BD Falcon) with 0.01 ml increments. Similarly for the thermal conductivity, the measurements were performed in a controlled temperature oven (Yamato-Scientific DKN602C, Santa Clara, CA) over a similar temperature interval with 15 min stabilizing times for each temperature. Thermal conductivity measurements were made with a Decagon Devices KD2 Pro thermal property measurement system (Pullman, WA). The specific heat measurements were performed using the TA Instruments DSC Q2000 (New Castle, DE) differential scanning calorimeter which is already automated to test small samples over a range of temperatures. The data was then parameterized as a function of temperature so that it could be incorporated into thermal simulations.

Bench top experiments in ex vivo bovine liver

To validate the computational model and evaluate the performance of the HeatSYNC gel in *ex vivo* tissue, we performed a set of ablations in room-temperature bovine liver. Specifically, $n = 3$ heating experiments are conducted in liver without the HeatSYNC gel and another $n = 3$ experiments in liver tissue with the injected HeatSYNC gel. All *ex vivo* experiments are performed with a custom 2.45 GHz water-cooled monopole applicator and with 50 W applied input power (assessed at the applicator connector) for 10 min. The applicator diameter is 2.1 mm and the outer shaft is made from polyimide. Room temperature water is circulated at a rate of 50 ml/min through the applicator.

The system setup is shown in Figure 2. Microwave power is passed from the generator (GMS 200 W, SAIREM Inc., France) *via* a 3 ft-long RG393 coaxial cable (attenuation ~0.12 dB/ft @2.45 GHz, Pasternack RF, Irvine, CA, USA) to a power meter (7022 Statistical, Bird, Solon, OH, USA), and continues through 3 ft-long RG400 coaxial cable (attenuation ~0.22 dB/ft @2.45 GHz, Pasternack RF) to the MW ablation applicator. A peristaltic pump (Masterflex L/S) was used to circulate ~20 °C room-temperature water through the applicator in a closed-loop flow circuit at a rate of approximately 50 ml/min.

Temperatures were measured at three discrete locations within the *ex vivo* liver tissue as depicted in Figures 2 and 3 with fiber optic sensors (Neoptix™ Reflex™, Canada LP).

Figure 3 also shows the custom built template, which facilitates repeatable positioning of an approximately $6 \times 6 \times 6\,cm^3$ section of liver tissue, the microwave ablation applicator, and fiber optic sensors. In pilot experiments within *ex vivo* tissue, it was observed that free injection of the HeatSYNC into *ex vivo* liver parenchyma would lead to spreading of the gel through the vessels that are air-filled in the *ex vivo* setting. In order to localize the gel at the time of injection, a cavity was created within the liver tissue sample using a Dremel tool, and the HeatSYNC gel was injected into the cavity using a 15 G needle. Needle was held in same position during injection and subtracted from cavity when gel fully filled the cavity. Ablations were commenced shortly ($<$ 5 min) after injecting the HeatSYNC gel into the cavity. The template facilitates sectioning of the tissue sample in a plane including the applicator shaft and the HeatSYNC gel, which allows for post-heating verification and measurement of the actual positioning of the applicator and fiberoptic probes relative to the location of injected gel. In ablation control experiments without the HeatSYNC gel, fiber optic sensor distal tips are set at radial distances of 4–5 mm (Channel 1), 4–5 mm (Channel 2), and 19–21 mm (Channel 3), respectively. For ablation experiments with the HeatSYNC gel, fiber optic sensor distal tips are set at radial distances of 4–4.5 mm (Channel 1), 4–6.0 mm (Channel 2), and 18.5–19 mm (Channel 3), respectively. Measured area of gel and specific positions of applicator and fiber optic probes from each experiment are subsequently used to set up corresponding geometries in computational models of microwave ablation with the thermal accelerant.

On completion of the ablation, the tissue was sectioned in a plane along the axis of the ablation applicator and the fiber optic temperature sensors. Tissue cross-sections with achieved ablation and solidified thermal accelerant (seen as the white region in Figure 3B), are digitally scanned using a flatbed scanner (Epson v550 Perfection) and ablation zones segmented with a custom algorithm implemented in MATLAB (R2020a). The segmentation approach consists of a two-step process, where the first step utilizes a *k*-means clustering algorithm applied to RGB space of the scanned image to separate the image into ablated/non-ablated areas. The second/final step smooths the separated areas of the image and filters out spurious regions marked as ablated tissue but that are not contiguous from the ablation zone.

Computational model of microwave absorption and heat transfer in ex vivo tissue

A coupled electromagnetics-bioheat transfer computational model was implemented in COMSOL Multiphysics (v5.6, COMSOL Inc., Burlington, MA) to study the effects of the HeatSYNC thermal accelerant on spatial and temporal distribution of temperature profiles in liver tissue. The model was adapted from models previously developed and experimentally validated in a range of tissue types [44,50,51]. Briefly, the model first solves for the time-averaged electric field

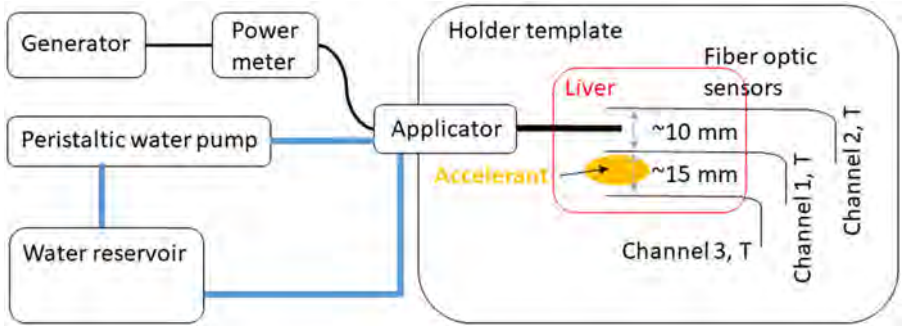

Figure 2. Setup for experimental ablation procedures in *ex vivo* bovine liver.

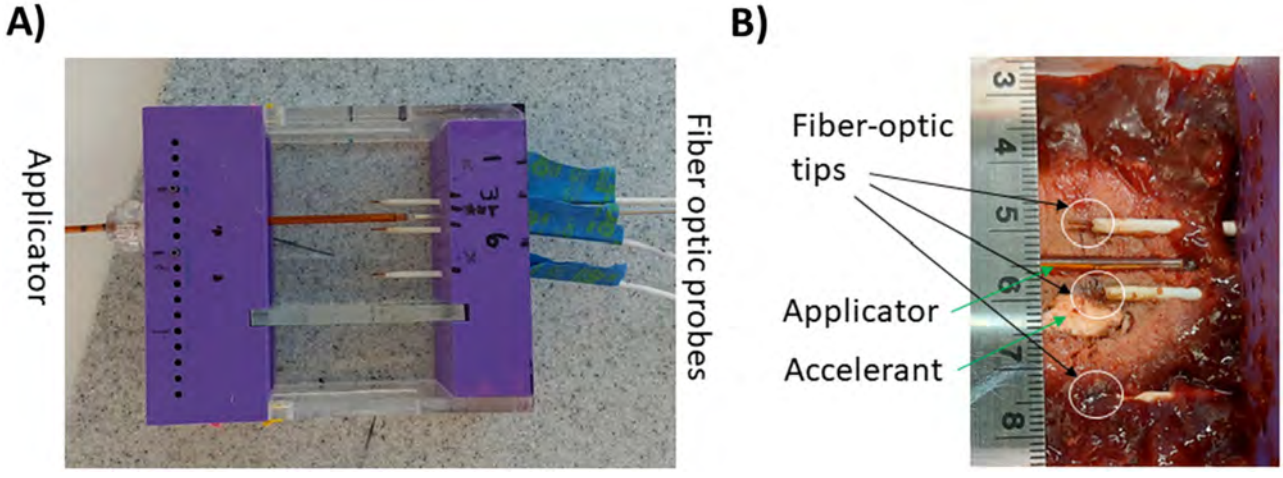

Figure 3. (A) Fixture template for holding liver sample, applicator and fiber optic probes and B) sample of position measurement of applicator and fiber optic probes with respect to injected gel after heating.

intensity in tissue using the time-harmonic electromagnetic Helmholtz wave equation:

$$\nabla^2\mathbf{E} + \beta_0^2\left(\varepsilon_r(T) - \frac{j\sigma(T)}{\omega\varepsilon_0}\right)\mathbf{E} = 0, \quad (1)$$

where **E** is the electric field intensity [V/m], β_0 is the wavenumber in free space [m^{-1}], $\varepsilon_r(T)$ is temperature-dependent relative permittivity [-], σ (T) is temperature-dependent effective electrical conductivity [S/m], ω is angular frequency [$rad \cdot s^{-1}$], and ε_0 is the permittivity of free space. The time-averaged power loss density, Q_{mw}, in all regions is determined using:

$$Q_{mw} = \frac{1}{2}\sigma(T)|\mathbf{E}|^2. \quad (2)$$

The incremental change in temperature at each time step is then determined with the transient heat transfer equation

$$\rho c(T)\frac{\partial T}{\partial t} = \nabla \cdot k(T)\nabla T + Q_{mw}, \quad (3)$$

where $\rho c(T)$ stands for temperature-dependent volumetric heat capacity [$J/m^3/°C$], and $k(T)$ is temperature-dependent thermal conductivity [W/m/°C]. We employ a transient solver with backward differentiating formula (BDF) of low order (maximum 2) and relative event tolerance 0.005. Time steps are adaptively chosen by the solver according to computation error and were no longer than 20 s.

The simulation domain consists of a cylinder of height 10 cm and diameter 8 cm, with material properties assigned to approximate bovine liver. The microwave applicator is positioned along the central axis of tissue cylinder, with the tip of the antenna positioned 1.35 cm above the cylinder base. In the case of simulations for comparison with *ex vivo* experiments, the microwave applicator is a water-cooled coaxial monopole operating at 2.45 GHz and monopole length 7.5 mm. Polyimide tubes (Zeus Inc., Orangeburg, SC, USA) of outer diameters ~1.3 mm and ~2.2 mm are used for water-inflow tube and outer applicator shaft respectively. The overall diameter of applicator is 2.2 mm. The thermal accelerant is modeled as ellipsoid with dimensions corresponding to the measurements from each individual experiment in *ex vivo* tissue as illustrated in Figure 4.

Initial tissue temperature for simulations mimicking *ex vivo* experimental conditions is $T = 25\,°C$. At all outer boundaries of simulation space, we apply a first order Sommerfeld radiation boundary condition

$$\mathbf{n} \times (\nabla \times \mathbf{E}) - jk\mathbf{n} \times (\mathbf{E} \times \mathbf{n}) = 0\ , \quad (4)$$

where **n** denotes unit normal vector to the corresponding simulation boundary, and thermal insulation boundary condition

$$\boldsymbol{n} \cdot (k\nabla T) = 0. \quad (5)$$

To approximate the internal water cooling of the microwave applicator, we employ a convective heat-flux boundary condition on outer shaft of the applicator

$$q_0 = h \cdot (T_{ext} - T). \quad (6)$$

with heat-flux coefficient $h = 200\,W/m^2/°C$ and external temperature $T_{ext} = 20\,°C$.

Material properties of the bovine liver are simulated as temperature dependent and their initial values at room temperature as well as functions for temperature dependency approximation are summarized in Table 1.

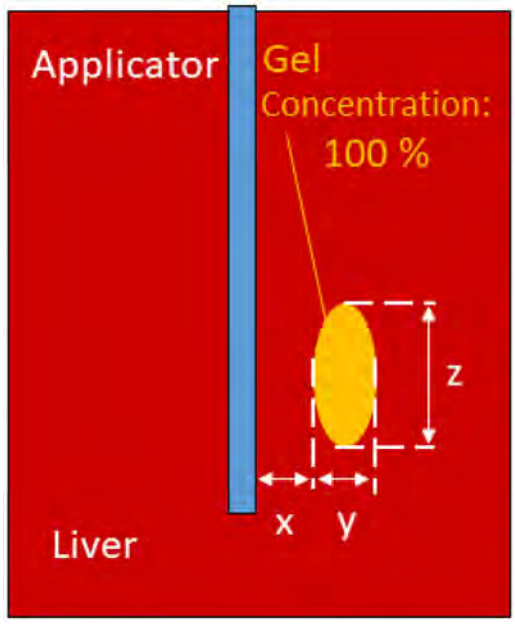

Figure 4. Geometry of simulation space for *ex vivo* simulations with the 2.45 GHz MWA applicator and the HeatSYNC gel.

Similarly, expressions for the dielectric and thermal properties of the HeatSYNC gel and their temperature dependencies are summarized in Table 2.

Extension and adaptation of the computational model for simulating ablations in vivo

Next, we employ the computational model to simulate ablation under *in vivo* conditions, similar to the conditions under prior experiments in porcine liver *in vivo* (from [30,34] and Theromics' internal results).

Thermal simulations are setup to solve the Pennes' bioheat transfer equation:

$$\rho c_i(T)\frac{\partial T}{\partial t} = \nabla \cdot k(T)\nabla T + Q_{mw} - \omega_{bl}(T)c_{bl}\rho_{bl}(T - T_{bl}). \quad (7)$$

where $\omega_{bl}(T)$ denotes temperature dependent blood perfusion coefficient (18e-3 [s^{-1}]), c_{bl} stands for specific heat capacity of blood (3617 [J/kg/K]) [52], ρ_{bl} is the density of blood (1050 [kg/m^3]) [52] and T_{bl} is physiologic blood temperature (37 °C). The value of $\omega_{bl}(T)$ is scaled by a factor 0.1 for regions with the thermal accelerant present, to approximate the impact of the accelerant on reduced blood flow. Furthermore, to approximate the effects of thermally induced microvascular stasis, $\omega_{bl}(T)$ is modeled as a smoothed step function, such that its value decreases to 50% of its initial value at 52.5 °C, and to $0\,s^{-1}$ at 60 °C [53]. While the Pennes' bioheat transfer model has acknowledged limitations [54,56], it remains an effective and widely used bioheat transfer model for simulating thermal ablation *in vivo* .

Example tissue sections, illustrating ablation zones with and without the HeatSYNC gel are provided in Figure 1. Unlike the conditions considered in *ex vivo* ablation

Table 1. Dielectric and thermal properties of bovine liver used in *ex vivo* simulations.

Property	Value @25 °C	T dependency function	Reference
ε_r [-]	46.17	Piecewise linear, frequency dependent fit [0.5 – 6 GHz]	[49]
σ [S/m]	1.795	Piecewise linear, frequency dependent fit [0.5 – 6 GHz]	[49]
ρc [J/m^3/°C]	4e6	$\rho c(T) = \begin{cases} \rho c, & T \in (25,\ 95) \\ \frac{\rho c + \rho c_v}{2} + \frac{\rho_w L C}{\Delta T}, & T \in (95,\ 105) \\ \rho c_v, & T > 105 \end{cases}$	[53–55]
k [W/m/°C]	0.454	$k(T) = \begin{cases} 0.49 + \Delta k(T-37), & T \in (25,\ 100) \\ 0.49 + \Delta k(100-37), & T > 100\ ^\circ C \end{cases}$	[47, 53, 55]

* ρc_v stands for volumetric heat capacity of vaporized tissue with value of 6e5 [J/m^3/°C], ρ_w is the density of water, L is latent heat of vaporization of water with value 2260 kJ/kg, C is the water content in tissue (0.73[-]), ΔT is temperature interval around boiling point of water, where vaporization takes place, and Δk is rate of change of thermal conductivity 0.003 [W/m/°C^2].

experiments where efforts were made to localize the HeatSYNC gel to a position lateral to the ablation applicator, the results from prior *in vivo* experiments suggest that the HeatSYNC gel impacts the ablation zone across the angular expanse. We did not anticipate the impact of the HeatSYNC gel would remain substantial on the contra-lateral side, if the HeatSYNC gel remained localized to the injection site. Thus, we considered two approximations as illustrated in Figure 5: (A1) modeled to approximate the HeatSYNC gel spread out over a broader volume following injection, but remains static over the course of the ablation procedure; and (A2) modeled to approximate the HeatSYNC gel that spreads over the course of an ablation when local temperature of the gel is in the range $40 < T < 55$ °C.

In vivo model approximation A1: we introduce a volume with mixture of tissue and thermal accelerant properties. Two mixtures are studied, the first with 50% of thermal accelerant and 50% of tissue (50/50 mixture) and the second with 10% of thermal accelerant and 90% of tissue. The material properties of the mixture are set as a weighted average of tissue and thermal accelerant properties with weights corresponding to ratio of tissue/thermal accelerant in the mixture volume. The mixture volume is simulated as a sphere with volume of thermal accelerant, which corresponded to 2 cm^3 (2 ml) divided by gel concentration in the mixture. The center of the mixture volume is placed on the applicator axis.

In vivo model approximation A2: This model was developed to approximate observations that the HeatSYNC gel viscosity generally decreased with increasing temperature from room temperature (~20 °C) to physiologic temperature (37 °C). As a first order approximation of the spread of the gel in regions with increasing temperature, we employed the following time and temperature dependent model of gel presence $gm(t,T)$ throughout the tissue domain:

$$gm(t,T) = \begin{cases} \exp\left(-4 \cdot \left(\frac{(x-x_0)^2}{x_s^2} + \frac{(y-y_0)^2}{y_s^2} + \frac{(z-z_0)^2}{z_s^2}\right)\right), & T < 40\ ^\circ C \\ 0, & 40\ ^\circ C \le T \le 55\ ^\circ C \\ 0, & 55\ ^\circ C < T \end{cases}, \quad (8)$$

Table 2. Parameterizations for temperature dependencies of the dielectric and thermal properties of the HeatSYNC gel.

Property	T dependency function
ε_r [-]	$\varepsilon_r\ (T) = \varepsilon_r + \Delta\varepsilon_r \cdot (T-25),\ T \in (25,\ 90)$
σ [S/m]	$\sigma\ (T) = \sigma + \Delta\sigma \cdot (T-25),\ T \in (25,\ 90)$
ρc [J/m^3/°C]	$\rho c(T) = \rho c + \Delta\rho c \cdot (T-25),\ T \in (25,\ 90)$
k [W/m/°C]	$k(T) = k + \Delta k_{TA} \cdot (T-25),\ T \in (25,\ 90)$

where $x_0,\ y_0,\ z_0 = (15\ mm,\ 0\ mm,\ 0\ mm)$ are initial coordinates of center of gel volume, and $x_s,\ y_s,\ z_s = (13 + 0.1 \cdot t,\ 13 + 0.1 \cdot t,\ 26 + 0.1 \cdot t)$ define initial dimensions of gel area and its spread over time [mm]. It is noted that this is a rough approximation, rather than a model derived formally from first principles, to evaluate the potential impact of gel spreading during heating on the ablation profile. Tissue dielectric thermal properties and blood perfusion are consequently set as the weighted average of tissue and gel properties. For example, for relative permittivity, the following expression was used:

$$\varepsilon_r = \varepsilon_{r_gel} \cdot gm(t,T) + \varepsilon_{r_tissue} \cdot (1 - gm(t,T)). \quad (9)$$

Blood perfusion coefficient ω_{gel} (i.e., in regions where $gm(t,T) = 0$) for gel was set to 0 $Wm^{-3}K^{-1}$.

Ablation boundary estimations. Transient temperature maps from simulations are used to estimate the ablation extents using the Arrhenius thermal damage and thermal iso-effective dose models. The Arrhenius thermal damage coefficient, Ω, is calculated with:

$$\Omega(ti) = \sum_{ti=1}^{Ti} \Delta t \cdot A e^{-\frac{E_a}{R \cdot T(ti)}}, \quad (10)$$

where A is the frequency factor (5.51e41 [s^{-1}] in liver), E_a is the activation energy (2.77e5 [J/mol] in liver) [55], R is the gas constant 8.3143 [J/mol/°C,] ti is time index, Ti is the total number of time-steps Δt, and $T(ti)$ is the temperature at time ti. We also calculate the thermal isoeffective dose, which translates an arbitrary time-temperature profile to

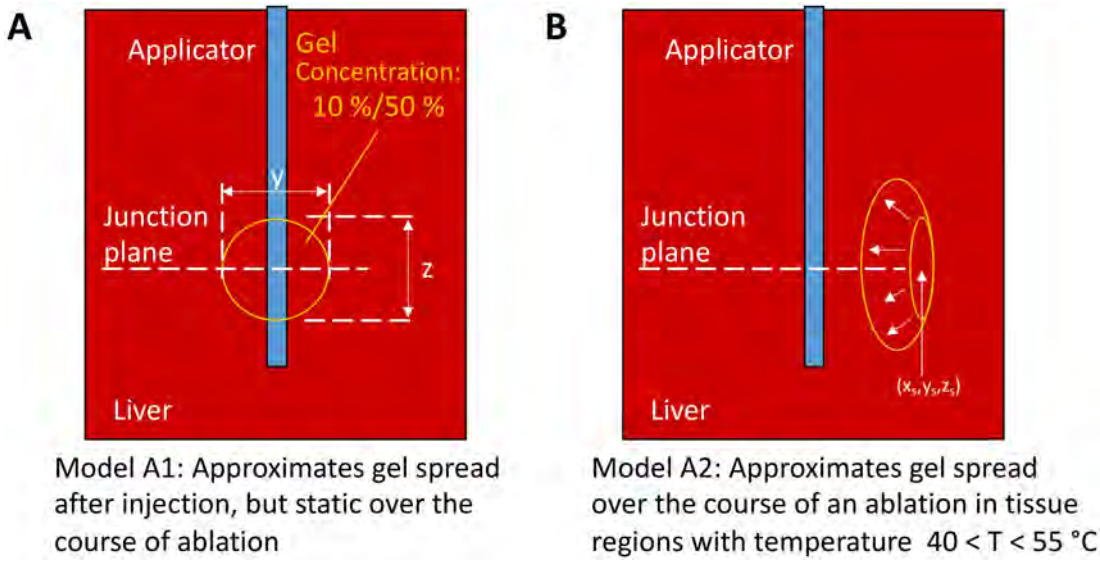

Figure 5. Geometries illustrating approximations used for modeling the impact of potential spread of the HeatSYNC gel on ablation profiles under *in vivo* conditions. (A) Model A1 – HeatSYNC gel spreads after injection, but remains static over the course of the ablation. (B) Model A2 – HeatSYNC gel spreads during the course of an ablation in tissue regions with temperature in the range $40 < T < 55\,^{\circ}C$.

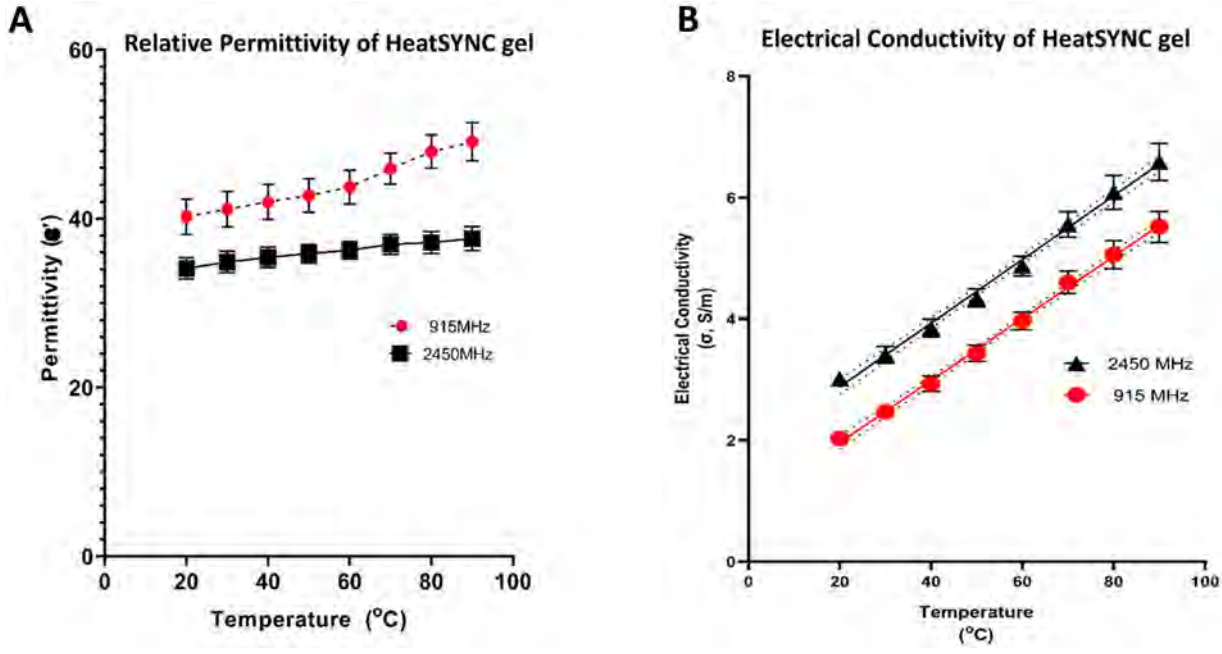

Figure 6. Temperature dependent dielectric properties of the HeatSYNC gel at 915 MHz and 2.45 GHz.

equivalent minutes of heating at 43 °C (CEM43) dose according to

$$CEM43(ti) = \sum_{ti=1}^{Ti} \Delta t \cdot R_{CEM}{}^{43-T(ti)}, \qquad (11)$$

where R_{CEM} is unit-less factor of 0.25 ($T < 43\,^{\circ}C$) and 0.5 ($T >= 43\,^{\circ}C$). The volume where $\Omega(ti) > 1$ and $CEM43(ti) > 240$ min is used to determine the extents of the ablation zone.

Results

Experimentally measured dielectric and thermal properties of the HeatSYNC gel

Figure 6 illustrates the temperature dependent relative permittivity and electrical conductivity of the HeatSYNC gel measured over the temperature range 20 – 90 °C.

Figure 7 illustrates the temperature dependent (A) density, (B) thermal conductivity, and (C) specific heat capacity of the HeatSYNC gel measured over the temperature range 20 – 90 °C.

Experimental ablations in ex vivo tissue

Figure 7A shows an example ablation zone along the applicator axis in *ex vivo* liver without the HeatSYNC gel present; Figure 7B–D illustrate example ablation zones with the HeatSYNC gel injected at a distance of 10 mm radially from the applicator surface. For all

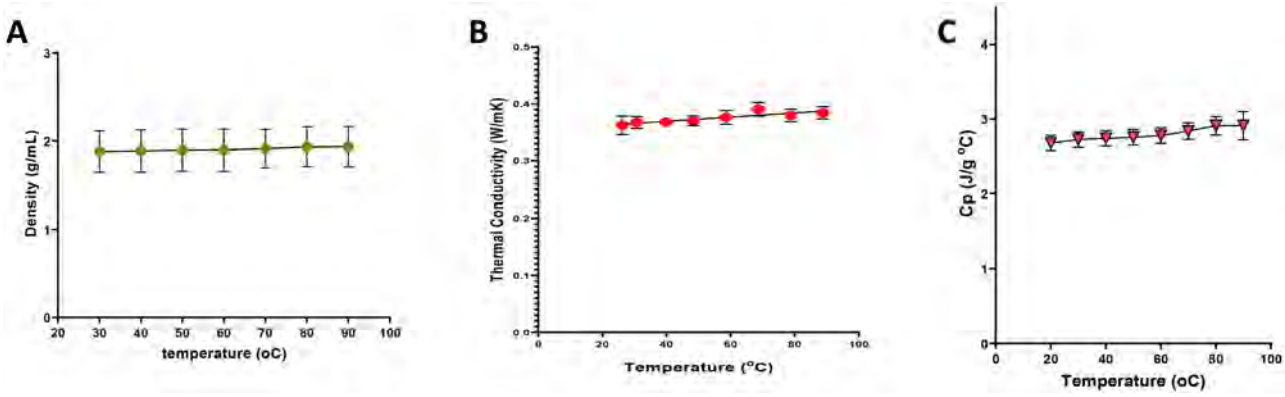

Figure 7. Temperature dependent thermal properties of the HeatSYNC gel: (A) density, (B) thermal conductivity, and (C) specific heat capacity.

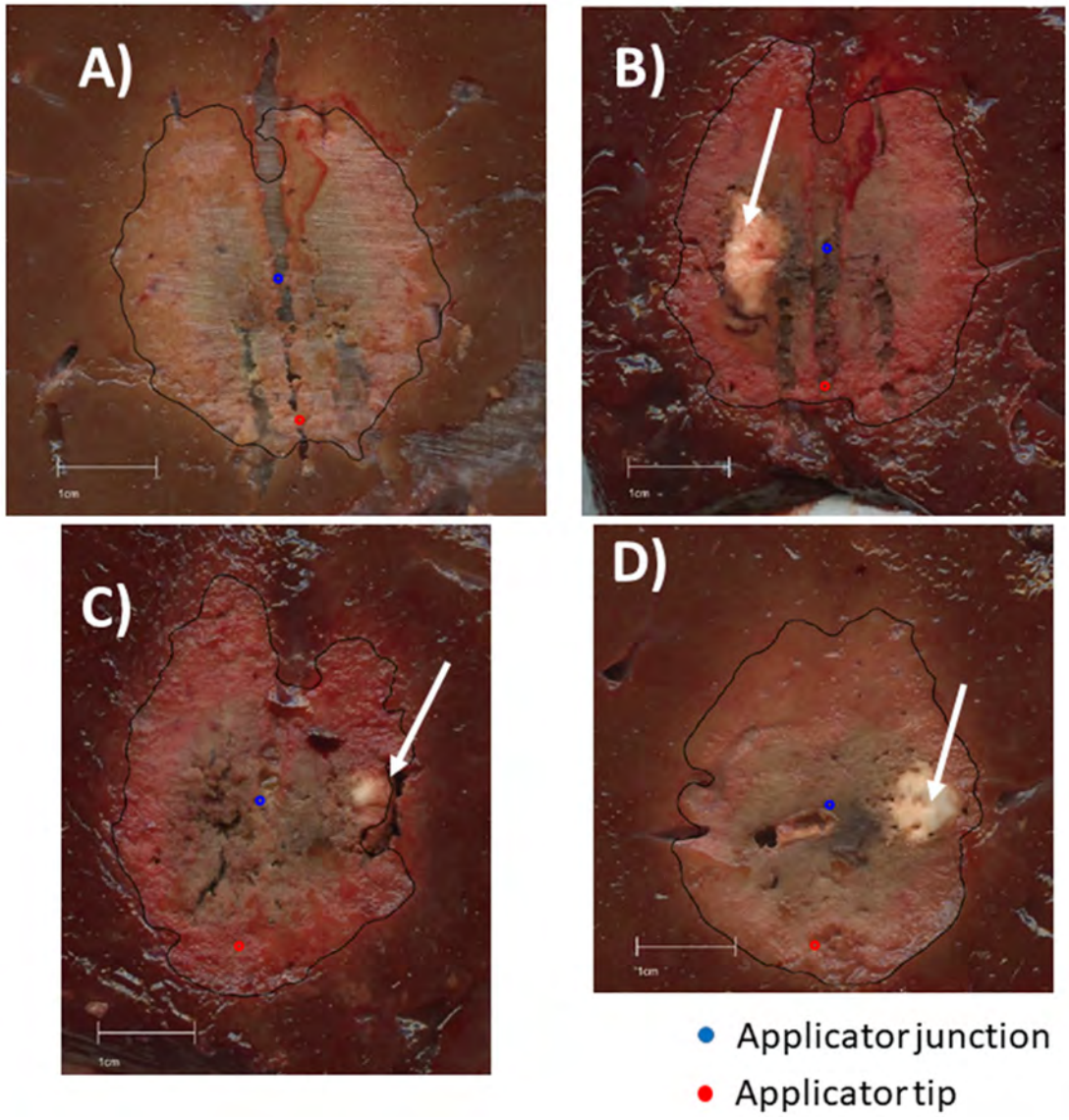

Figure 8. Ablation extents as observed in tissue cross-section after experiments (black contours). Depicted cases include case without thermal accelerant gel (a), and experiments 1 (B), 2 (C), and 3 (D) with present thermal acceleration gel. White arrows mark the position of gel. White labels in the lower left corner label 1 cm distance within image.

figures, ablations are conducted with 50 W power applied for 10 min using a 2.45 GHz water-cooled monopole antenna.

The white mass visible in Figure 8 is the solidified thermal accelerant. This phase change from liquid to solid takes place between 60 °C and 70 °C.

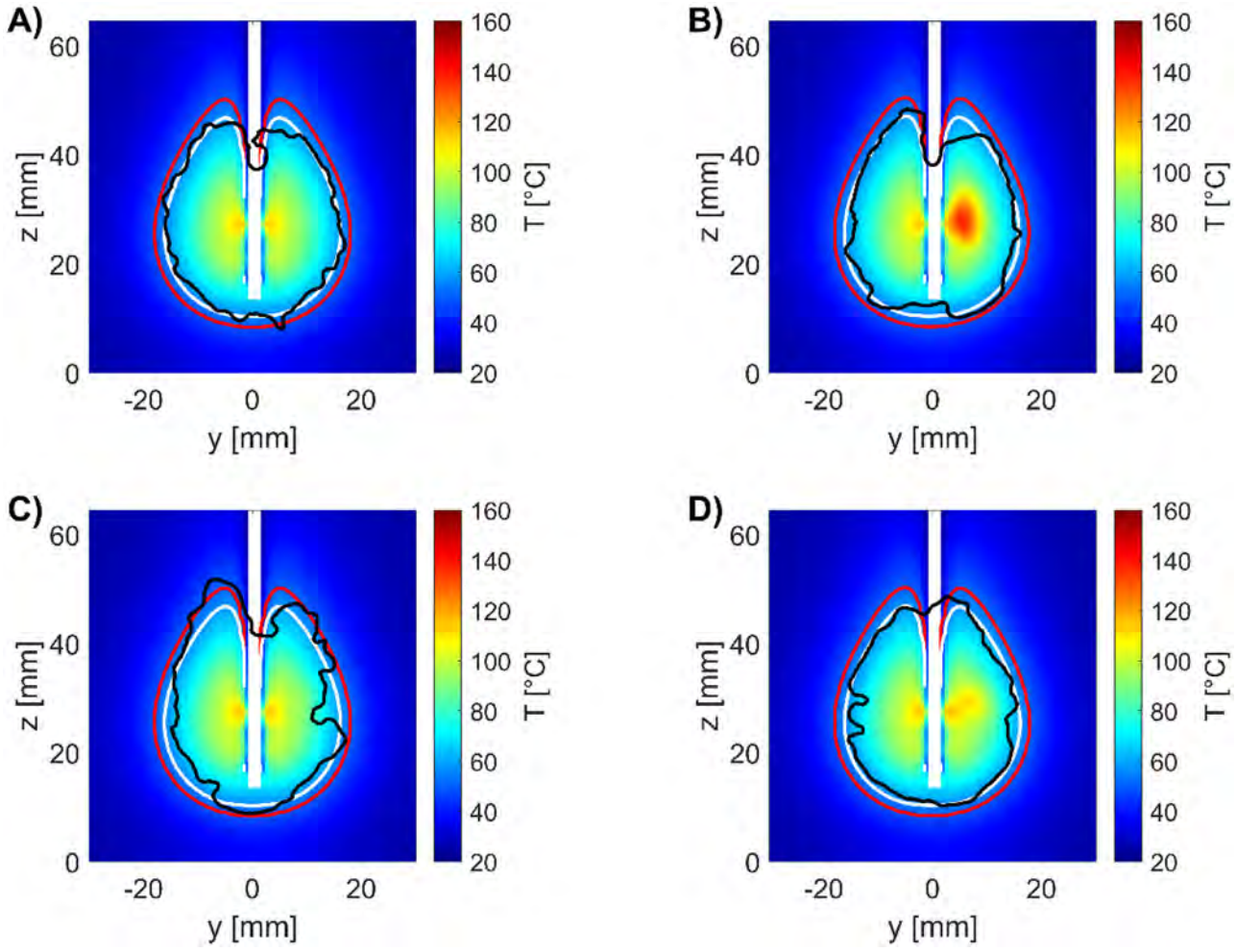

Figure 9. Ablation extents as observed in tissue cross-section after experiments (black contours) and as predicted by simulation, specifically 240 CEM43 (red contours) and Arrhenius thermal damage model for liver whitening (white contours). Depicted cases include case without thermal accelerant gel (A), and experiments 1 (B), 2 (C), and 3 (D) with present thermal acceleration gel, respectively.

Table 3. Extents of the ablation zone from experiments in *ex vivo* bovine liver and corresponding simulations, when Arrhenius thermal damage is used for extents prediction.

	W_1 [mm]	W_2 [mm]	H [mm]
Control	33.4	–	37.8
Control, simulation	31.5	31.5	36
Exp. 1, measurement	32.1	–	38.3
Exp. 1, simulation	31.5	31.5	36
Exp. 2, measurement	31.9	–	43
Exp. 2, simulation	31.5	31.5	36
Exp. 3, measurement	30.9	–	38.4
Exp. 3, simulation	31.5	31.5	36
Mean ± STD, Measurement	32.9 ± 2.6	–	40.2 ± 2.3
Mean ± STD, Simulation	31.5 ± 0	31.5 ± 0	36 ± 0

Ablation experiments considered 50 W power applied for 10 min.

Figure 9 shows simulated temperature profiles in *ex vivo* liver corresponding to experiments where the HeatSYNC gel is not present (Figure 8A) and where it is present (Figure 8B–D), respectively, with 50 W applied for 10 min using a 2.45 GHz water-cooled monopole antenna. Also included are estimated extents of the ablation zone with the thermal dose and Arrhenius thermal damage models, as well as the extent of the thermal ablation zone from experiments. Note that for each simulation resulted presented in Figure 9B–D, the position of the HeatSYNC gel in the model was determined from the estimated position of the gel observed in the corresponding experiment in *ex vivo* liver (Figure 8B–D).

The measurements of the diameter (W1 and perpendicular W2) and height (H) along the applicator axis of the ablation zone from simulations and corresponding experiments are summarized in Table 3.

Figure 10 illustrates transient temperature profiles, which are captured at locations of fiber optic probes (Channel 1, Channel 2, and Channel 3) during 50 W, 10 min ablation experiments in *ex vivo* bovine liver with and without the HeatSYNC gel.

These transient temperature profiles are compared against the temperatures from simulations for three performed control experiments (without gel, Figure 11A, B, and C) and for three cases with injected thermal accelerant and results are shown in Figure 11D, E, and F.

Figure 12 shows simulated radial temperature profiles at various time points along ablation duration for *ex vivo* experiment 1 with thermal accelerant location shown in Figure 7B. Temperatures are shown along the line, which goes through middle point of thermal accelerant and is perpendicular to the applicator shaft.

Ablation extents as predicted for the porcine liver *in vivo* scenario A1 with the 2450 MHz applicator and with thermal

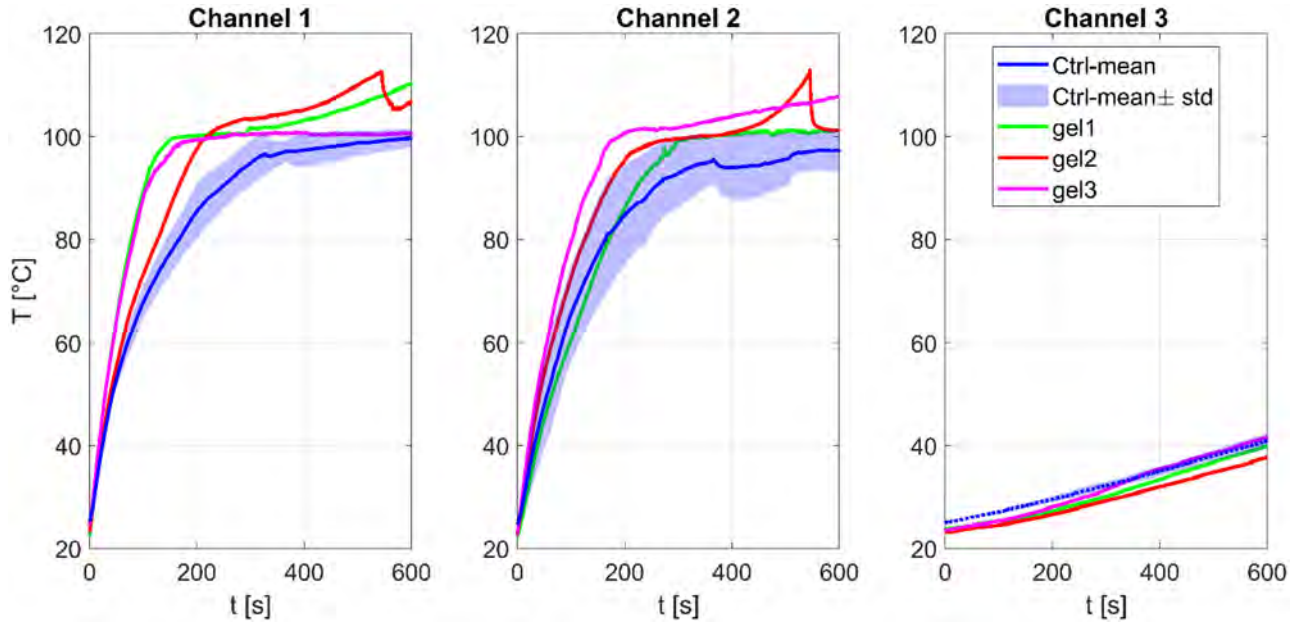

Figure 10. Transient temperature profiles as measured in respective fiber optic channel locations in *ex vivo* bovine liver tissue. legend symbol 'ctrl-mean' stands for average temperature curve from control experiments (without gel) and 'std' denotes standard deviation. Channel 1 is located 5 mm away from applicator shaft just in front of volume with thermal accelerant, channel 2 is placed 5 mm away from applicator at opposite side of applicator and channel 3 is 15 mm away from the applicator just behind the thermal accelerant.

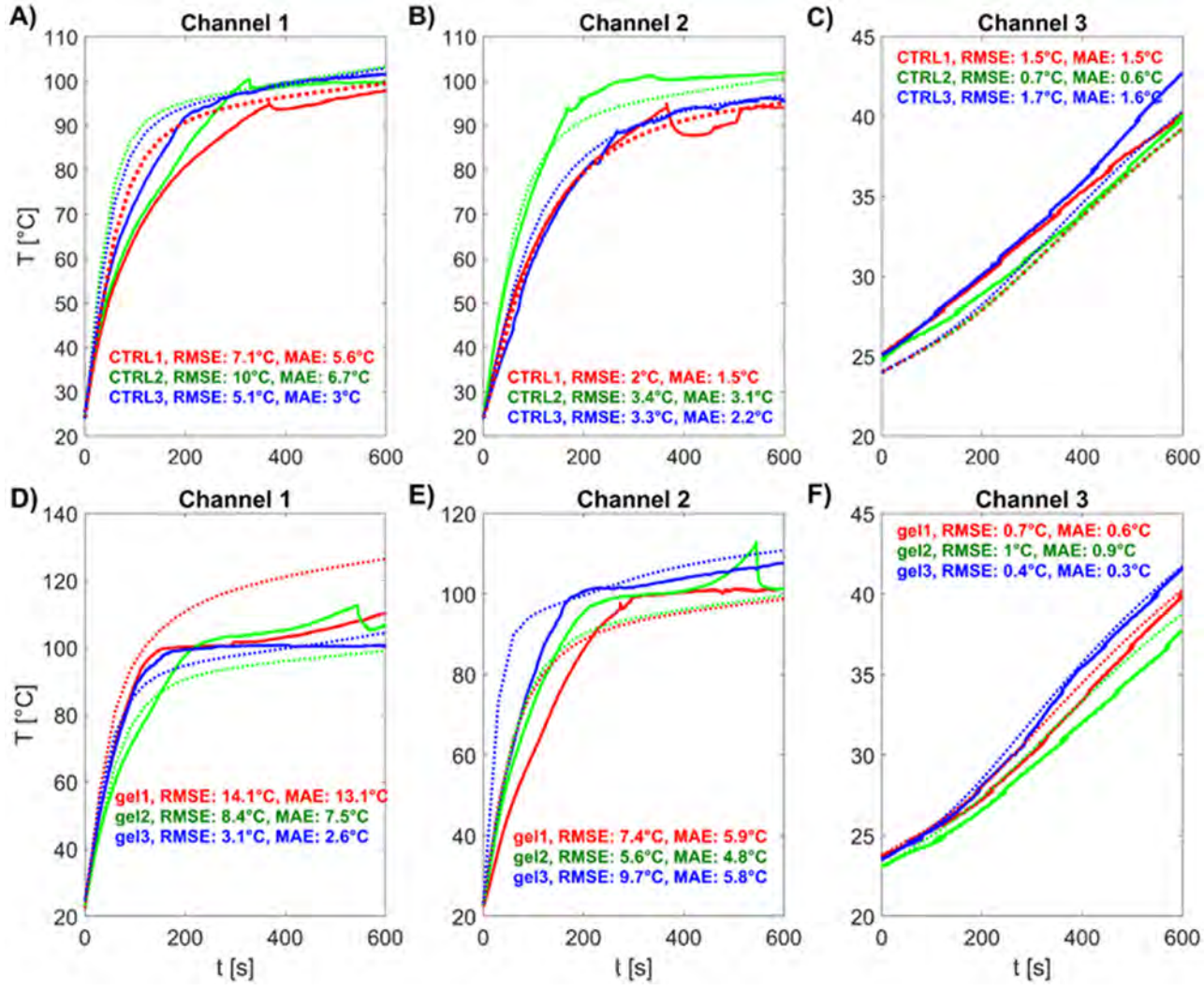

Figure 11. Comparison of simulated (dotted lines) vs measured (solid lines) transient temperature profiles in *ex vivo* bovine liver tissue without (A, B, and C) and with (D, E, and F) the HeatSYNC gel during 50 W, 10 min microwave ablation with a water-cooled 2.45 GHz antenna.

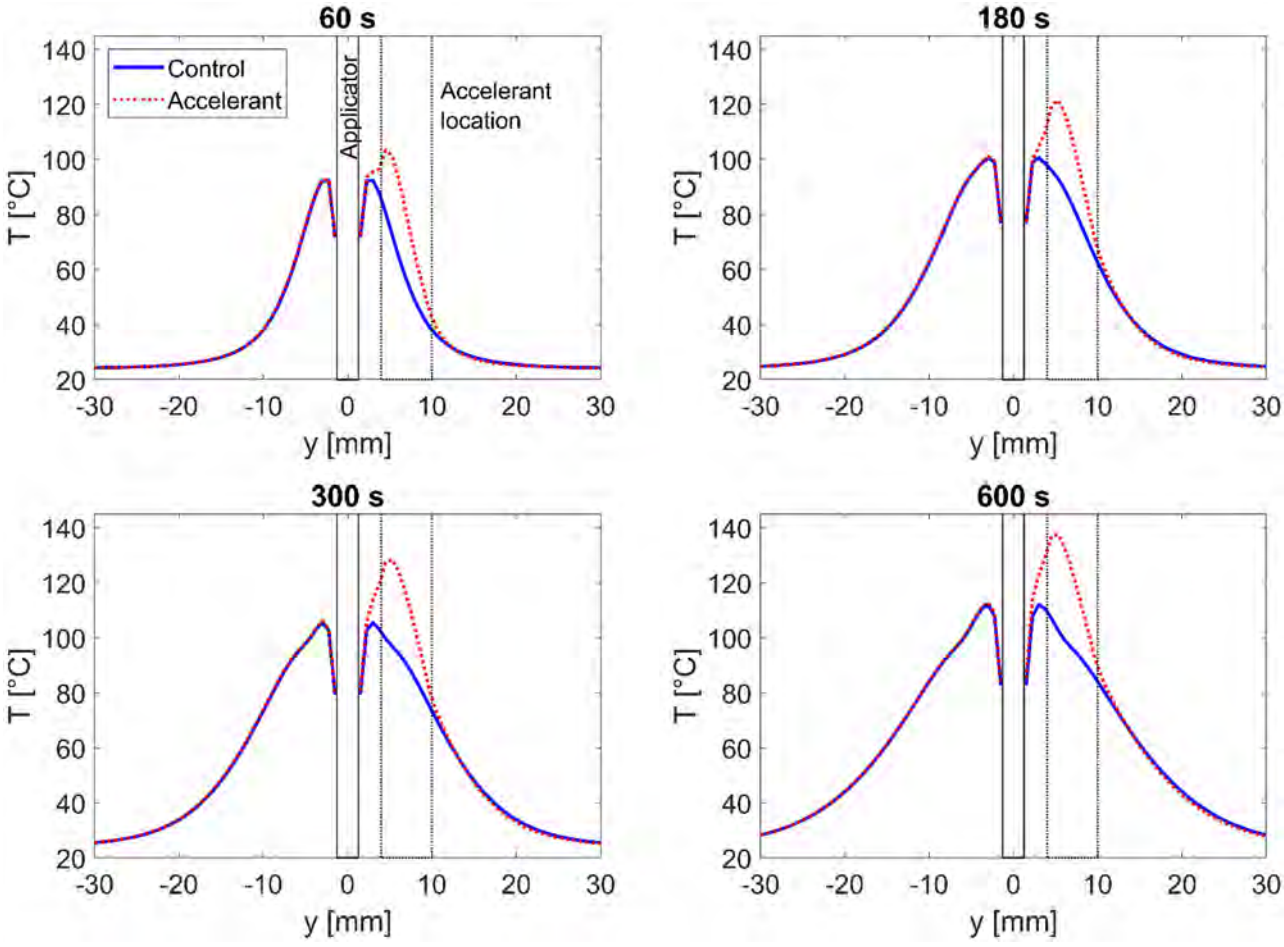

Figure 12. Simulated radial temperature profiles at 60, 180, 300 and 600 s after start of ablation experiment with thermal accelerant location shown in Figure 8B.

accelerant distribution in tissue over a broad volume are illustrated in Figure 13A, C (90% tissue, 10% gel) and Figure 13B, D (50% tissue, 50% gel), respectively. Consistent with the corresponding *in vivo* experiments from previous studies [30,33], these simulations consider 50 W applied for up to 10 min.

Figure 14 shows ablation extents as predicted for the porcine liver *in vivo* scenario A2 with the 2450 MHz applicator and transient gel distribution in tissue.

Values of the predicted ablation extents under *in vivo* conditions along three orthogonal axes are provided in Table 4.

Discussion

Prior studies have demonstrated the feasibility of enhancing microwave ablation volumes in a range of tissue types with the use of a thermal accelerant, such as the HeatSYNC gel. The present study was undertaken to develop a computational model for predicting the extent of microwave ablation zones in liver tissue when ablations are performed in conjunction with the HeatSYNC gel. The temperature-dependent dielectric and thermal properties of the gel are experimentally measured and implemented within computational bioheat transfer models. Model-predicted extents of the ablation zone were compared against measurements in *ex vivo* bovine liver tissue under similar conditions, as well as against measurements from prior ablation studies for *in vivo* porcine liver.

Measurements of the dielectric properties of the HeatSYNC gel at both 915 MHz and 2.45 GHz (Figure 6) show that the electrical conductivity of the HeatSYNC gel is substantially higher than that of liver tissue at room temperature. At 2.45 GHz, the electrical conductivity of the HeatSYNC gel is approximately 83% higher than that for liver tissue at room temperature, indicating greater absorption can be anticipated in the gel. Moreover, as the HeatSYNC gel is heated to temperatures up to 90 °C, the electrical conductivity of the gel increases nearly linearly with temperature, in contrast to the dielectric properties of liver tissue that tend to drop with increasing frequency, with a rather sharp drop at temperatures exceeding ~80 °C [45,46,49]. These measurements indicate that preferential microwave absorption within the HeatSYNC gel relative to tissue increases substantially as the gel heats up during an ablation procedure. The thermal conductivity of the gel is approximately 20% lower than liver tissue (Figure 7B), and the volumetric heat capacity is approximately 40% lower (Figure 7C) at room temperature. These imply that the gel will generally tend to retain the heat locally more than liver tissue. Transient temperature profiles measured within the HeatSYNC gel when confined within a tube, and corresponding temperature measurements without

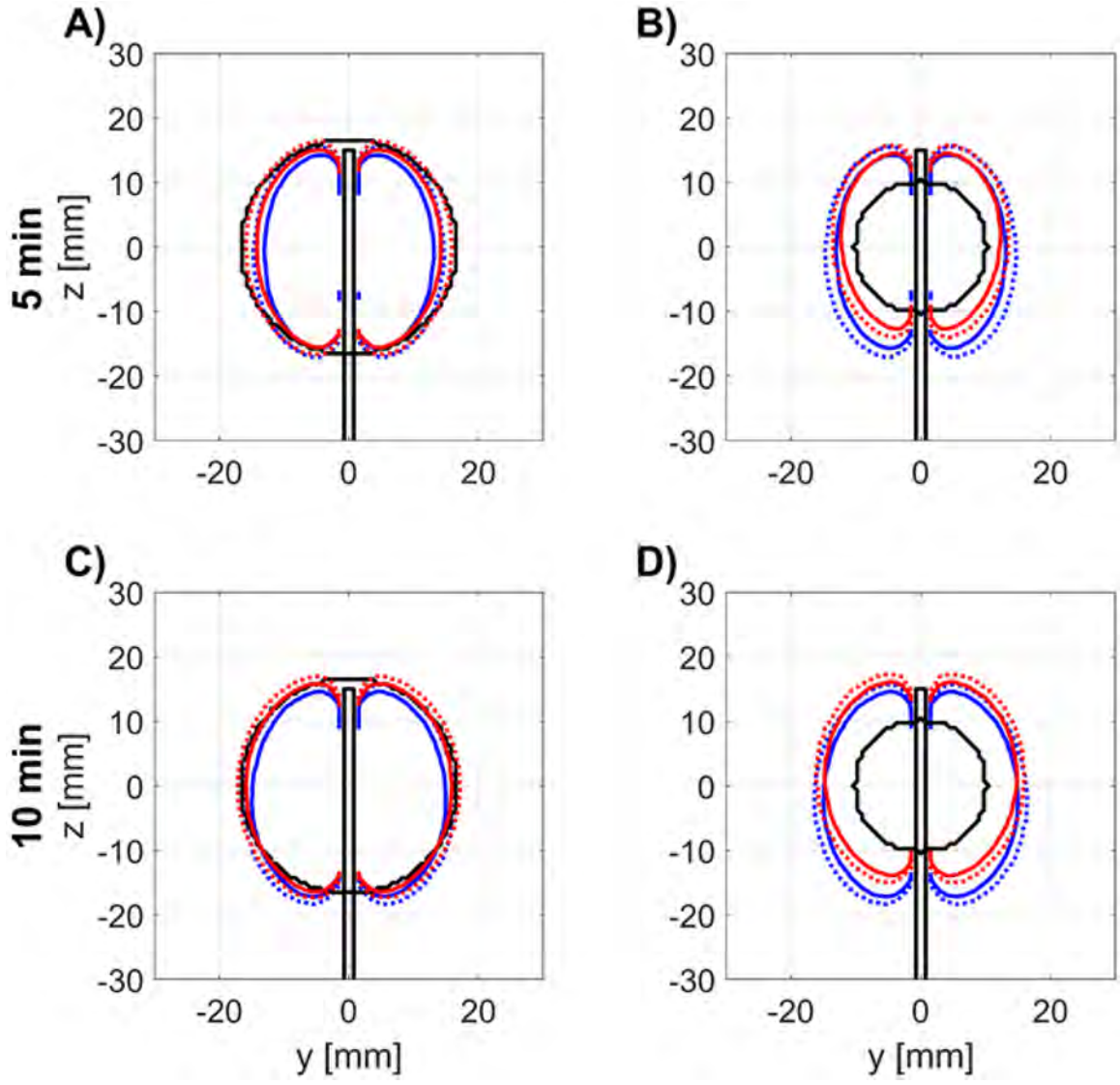

Figure 13. Sample of ablation extents estimated by 240 CEM43 (dotted lines) and Arrhenius thermal damage model with liver whitening kinetic parameters (solid lines). in case of *in vivo* liver without the HeatSYNC gel (blue line) and with the HeatSYNC gel (red line) at following ablation with a 2450 MHz applicator using 50 W applied for 5 min (a and B) and 10 min (C and D), respectively. Position of the gel/tissue mixture (90% tissue, 10% gel in a), C), and 50% tissue, 50% gel in B), D)) is illustrated with the black contour.

the HeatSYNC gel illustrated the greater local absorption and heating to higher maximum temperatures within the HeatSYNC (see Appendix, Figure A2).

As can be seen from the data in Figures 6 and 7, the changes in properties after the gel solidified (at approximately ~80 °C) were generally minimal. The two that showed any noticeable changes were the relative permittivity for the 915 MHz measurements and the specific heat capacity (C_p). For the former, the relative permittivity demonstrated a fairly constant increase from 20 to 60 °C as a function of temperature. After the solidification process (between 60 and 70 °C), the relative permittivity increased at a slightly greater, but relatively constant, rate. Similarly for the specific heat capacity, it also increased at a slight, but constant rate from 20 to 60 °C as a function of temperature. Only after the solidification process did the slope of the specific heat capacity increase as a function of temperature. In the case of the specific heat capacity, the changes were relatively subtle. For all of the other properties, there does not appear to be any noticeable changes in the trends with respect to temperature after the solidification process.

These material property data suggest that when a contiguous volume of gel is positioned in proximity to the ablation applicator where considerable microwave power is incident on the gel, substantially greater tissue temperatures can be anticipated in the gel as compared to tissue regions at a similar distance from the applicator. Conversely, when a contiguous volume of gel is positioned at regions further away from the ablation applicator (i.e., in regions where the thermal ablation zone spreads primarily by thermal conduction), the lower thermal conductivity may act to limit the spread of the ablation profile.

Transient temperature profiles measured in *ex vivo* bovine liver tissue (Figure 10) with the fiberoptic sensor positioned proximal to the gel in the radial direction from the ablation applicator (Channel 1) indicate a more rapid rate of heating, 0.61 °C/s, and higher maximum temperature (exceeds ~100 °C) compared to control, 0.27 °C/s and maximum

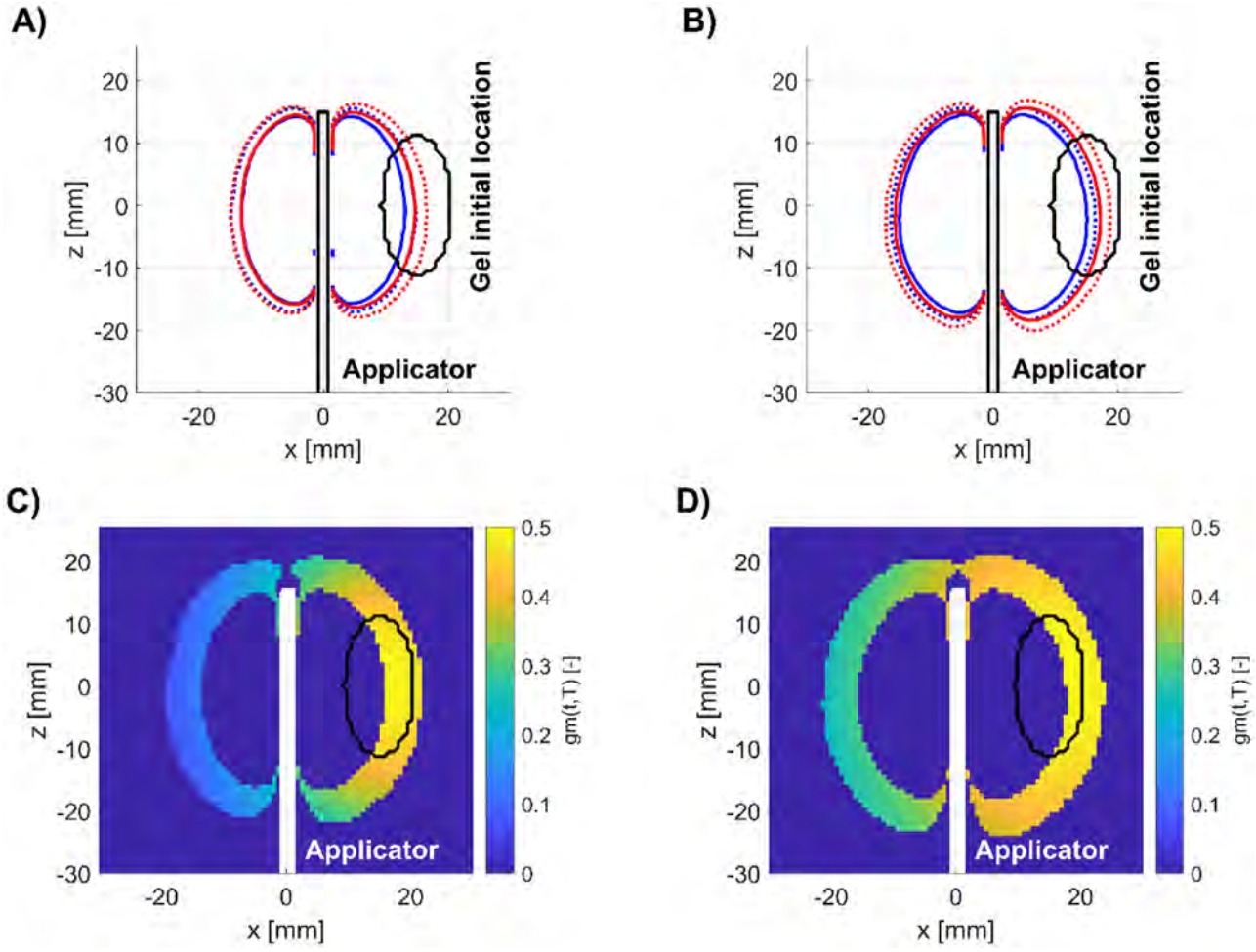

Figure 14. Simulated ablation extents (A, B) and gel distribution (C, D) in tissue at 5 (A, C) and 10 min (B, D). ablation extents are estimated by 240 CEM43 (dotted lines) and Arrhenius thermal damage of 63% (solid lines) with (red lines) and without present HeatSYNC gel (blue lines).

Table 4. Simulated extents (W1, W2 being maximum and minimum diameter) of the ablation zone following 50 W heating with the 2450 MHz microwave ablation applicator for 5 and 10 min in porcine liver *in vivo*, with and without the HeatSYNC gel.

	5 min				10 min			
	W_1 [mm]	W_2 [mm]	Height [mm]	Volume[cm^3]	W_1 [mm]	W_2 [mm]	Height [mm]	Volume [cm^3]
Control, simulation (no gel)	28.5	28.5	31.5	15.86	31.5	31.5	33	20.36
Approximation A1, 50% gel	26.25	27	28.5	12.12	31.5	31.5	30.75	20.36
Approximation A1, 10% gel	31.5	31.5	32.25	18.5	33	33	33.75	22.2
Approximation A2	30	30.7	33	18.39	34.5	35.2	36	26.26

temperature does not exceed 100 °C (i.e., measurement at the same location in experiments without the gel present). On the contra-lateral side of the ablation applicator (i.e., in the direction away from the gel; Channel 2), rate of heating for experiments with the gel present is 0.50 °C/s compared to 0.26 °C/s in control experiments, with similar observations in maximum temperature as for Channel 1. At a distance of ~20 mm from the ablation applicator in the direction of the HeatSYNC gel (i.e., beyond the gel), temperatures are consistent (and slightly lower) with measurements from control simulations. These observations are in alignment with the impact the gel would be anticipated to have based on the dielectric and thermal property measurements.

Model-predicted transient temperature profiles were generally in alignment with experimental measurements across the three measurement locations when considering ablation without (Figure 11A, B, C) and with (Figure 11D, E, F) the HeatSYNC gel, with mean absolute error (MAE) ranging between 1.5 °C – 5.8 °C for the no gel case, and between 0.3 °C – 11 °C with the HeatSYNC gel present, respectively. The greater variability between predicted and experimentally measured temperatures for cases with the HeatSYNC gel present may be in part due to differences in the idealized ellipsoidal shape profile of the gel used in simulations and the actual shape profile of the gel in experiments. Spread/migration of the gel during heating was not accounted for in the simulations of ablation under *ex vivo* conditions. The extents of the ablation zone predicted by the computational model and experimentally observed in *ex vivo* tissue were in good agreement (model: 31.5 ± 0 mm × 36 ± 0 mm vs. experiment: 32.9 ± 2.6 × 40.2 ± 2.3 mm).

While both the experiments in *ex vivo* tissue and the computational model predict similar thermal profiles and ablation zones in *ex vivo* tissue when using the HeatSYNC gel compared to ablations without the HeatSYNC gel, these findings are in contrast to observations from prior *in vivo* experimental studies [34] which indicated considerably larger ablation volumes when using the HeatSYNC gel (e.g., up to 50% larger in liver tissue [30]). Indeed, as seen in Figure 1, the ablation zone observed *in vivo* was generally larger circumferentially around the applicator axis, not just on the side for which the HeatSYNC gel was injected. Given the substantially higher microwave absorption in the HeatSYNC gel compared to liver tissue, we hypothesize that the use of the HeatSYNC gel may yield larger ablation profiles if it spreads out over a relatively large region. For the *ex vivo* tissue experiments, the gel remained in a constant volume cavity, and the corresponding scenario was modeled in simulations. However, in prior *in vivo* experiments, the gel was injected directly into liver parenchyma. We constructed computational models to simulate ablation zone profiles in liver under *in vivo* conditions (i.e., with perfusion included and with an initial temperature of 37 °C) with the gel spread out over a larger region to approximate a liver/HeatSYNC gel mixture, considering two scenarios. Models of the first scenario (Model A1), were constructed to approximate the gel spreading out within liver tissue following injection into the parenchyma but remaining in a static position over the course of the ablation. We considered 50% liver/50% gel and 90% liver/10% gel mixtures. In the second scenario, model A2, we attempted to approximate the transient spread of gel as a function of temperature, to emulate observations that the HeatSYNC gel viscosity generally decreased with increasing temperature, before congealing at ~70 °C. These simulations were conducted at 2.45 GHz, similar to ablation experiments conducted earlier studies in porcine liver *in vivo*, where not only volume but linear dimensions of ablation extents were recorded with MRI thermometry [34]. For modeling scenario A2, it is noted that in the absence of any heating (e.g., if the gel is injected and heat is not applied), the gel would not diffuse per the current approximate model.

For modeling scenario A1 with 10% gel mixture in liver, short axis diameter increased by up to 5% at 10 min, compared to control, and the height of the ablation zone increased by 2%. When simulating 50% gel mixture in tissue, no appreciable change in ablation extents was observed. These results suggest that spread of the gel prior to the ablation, but with the gel remaining static during the course of the ablation, has limited impact on overall volume of ablation zone. For modeling scenario A2, at 10 min, simulation results indicate a 9.5–11.7% increase in ablation zone short axes diameters, 11.7% increase in height of the ablation zone, and 28.9% increase in volume of ablation extents when compared to control. A prior experimental study in porcine liver *in vivo* with a clinical 2.45 GHz MWA applicator (100 W at generator; power applied for 10 min) showed that short axis diameters of the ablation zone as measured by MRI thermometry increased by 19.4–24.7% and height of the ablation zone increased by 7.4% when using the HeatSYNC gel compared to no gel control; a 39.6% increase in volume of the ablation zone was observed [34]. It is noted that the computational models reported here employed a 2.45 GHz water-cooled monopole antenna, which may differ from the proprietary antenna design used in the epxerimental studies. While the increase in short axis diameters and volume of ablation zones predicted by these models are smaller than those observed experimentally on MRI thermometry, these results suggest a potential role of the HeatSYNC spread during the course of the ablation in augmenting ablation profiles. Further studies are warranted to model spread of the HeatSYNC gel during ablation based on first principles, and to experimentally assess potential spread of the gel during ablation with suitable imaging techniques. Our studies to date have not considered the impact of spatially distributing gel injection sites (e.g., in quadrants), which may offer another degree of freedom for shaping ablation profiles. Further refinement and validation of the model is anticipated to support comparative assessments of the impact of HeatSYNC gel injection parameters (e.g., volume of gel injected; number of gel injection sites; gel injection location(s) relative to the ablation applicator; applied power/-time; others) for various treatment scenarios. The role of injection needle on ablation profile would also be of interest; during our preclinical pig studies, we have used a variety of needle types, including: 10 cm 5 Fr 19 G YUEH centesis needle (COOK Medical) with a hand-held pump (10 ml injection capacity), and a 19 G Luer lock needle with 1 ml syringe without a pump. Smaller (15–18 G) Luer lock needles can be readily used with a 3–5 ml syringe.

Overall, the experiments and computational models reported in this study contribute to an improved understanding of microwave absorption and heat transfer during ablation with the HeatSYNC gel present. The computational model predictions of ablation zones and temperature profiles in *ex vivo* tissue are generally aligned with experimental measurements. While the computational model of the *in vivo* scenario with the gel spreading during ablation offers a plausible mechanism by which the HeatSYNC gel contributes to larger ablation zones *in vivo*, further experimental studies are warranted to investigate this hypothesis. Future attempts at modeling should more carefully consider the shape profile of the gel following injection into tissue and during the course of the ablation, as well as impacts of tissue shrinkage (both with and without the HeatSYNC gel) on ablation profiles. Modeling efforts would also benefit from experimental characterization of the HeatSYNC gel viscosity as a function of temperature. The contributions of possible impact of the presence of the gel on blood perfusion rates also merits further investigation.

Acknowledgments

We acknowledge Prof. B. Stuart Trembly, a valued collaborator who passed away in 2021.

Disclosure statement

W.K.C.P. is a co-founder and Chief Scientific Officer for Theromics, Inc. D.E.D. is a co-founder and Chief Medical Officer for Theromics, Inc.

Funding

This work was supported by NSF STTR Phase I Award ID 2126555 to Theromics, Inc.

ORCID

Jan Sebek http://orcid.org/0000-0002-2116-6697
William K. C. Park http://orcid.org/0000-0002-8599-2613
Douglas W. Van Citters http://orcid.org/0000-0001-8914-1878
Punit Prakash http://orcid.org/0000-0001-6467-722X

Data availability statement

The data that support the findings of this study are available from the corresponding author, P. P., upon reasonable request.

References

[1] Ahmed M, Brace CL, Lee FT, et al. Principles of and advances in percutaneous ablation. Radiology. 2011;258(2):351–369. doi:10.1148/radiol.10081634.

[2] Gillams A, Goldberg N, Ahmed M, et al. Thermal ablation of colorectal liver metastases: a position paper by an international panel of ablation experts, the interventional oncology sans frontières meeting 2013. Eur Radiol. 2015;25(12):3438–3454. doi:10.1007/s00330-015-3779-z.

[3] Seror O. Ablative therapies: advantages and disadvantages of radiofrequency, cryotherapy, microwave and electroporation methods, or how to choose the right method for an individual patient? Diagn Interv Imaging. 2015;96(6):617–624. doi:10.1016/j.diii.2015.04.007.

[4] Wells SA, Hinshaw JL, Lubner MG, et al. Liver ablation: best practice. Radiol Clin North Am. 2015;53(5):933–971. doi:10.1016/j.rcl.2015.05.012.

[5] Ahmed M, Solbiati L, Brace CL, et al. Image-guided tumor ablation: standardization of terminology and reporting criteria–a 10-year update. Radiology. 2014;273(1):241–260. doi:10.1148/radiol.14132958.

[6] Haroon M, Sathiadoss P, Hibbert RM, et al. Imaging considerations for thermal and radiotherapy ablation of primary and metastatic renal cell carcinoma. Abdom Radiol (NY). 2021;46(11):5386–5407. doi:10.1007/s00261-021-03178-6.

[7] Nabavizadeh N, Jahangiri Y, Rahmani R, et al. Thermal ablation versus stereotactic body radiotherapy after transarterial chemoembolization for inoperable hepatocellular carcinoma: a propensity Score-Weighted analysis. AJR Am J Roentgenol. 2021;217(3):691–698. doi:10.2214/AJR.20.24117.

[8] Chu KF, Dupuy DE. Thermal ablation of tumours: biological mechanisms and advances in therapy. Nat Rev Cancer. 2014;14(3):199–208. doi:10.1038/nrc3672.

[9] Liu Y, Li S, Wan X, et al. Efficacy and safety of thermal ablation in patients with liver metastases. Eur J Gastroenterol Hepatol. 2013;25(4):442–446. doi:10.1097/MEG.0b013e32835cb566.

[10] Lubner MG, Brace CL, Hinshaw JL, et al. Microwave tumor ablation: mechanism of action, clinical results, and devices. J Vasc Interv Radiol. 2010;21(8 Suppl):S192–S203. doi:10.1016/j.jvir.2010.04.007.

[11] Andreano A, Brace CL. A comparison of direct heating during radiofrequency and microwave ablation in ex vivo liver. Cardiovasc Intervent Radiol. 2013;36(2):505–511. doi:10.1007/s00270-012-0405-1.

[12] Di Vece F, Tombesi P, Ermili F, et al. Coagulation areas produced by cool-tip radiofrequency ablation and microwave ablation using a device to decrease back-heating effects: a prospective pilot study. Cardiovasc Intervent Radiol. 2014;37:723–729.

[13] Hoffmann R, Rempp H, Erhard L, et al. Comparison of four microwave ablation devices: an experimental study in ex vivo bovine liver. Radiology. 2013;268(1):89–97. doi:10.1148/radiol.13121127.

[14] Livraghi T, Meloni F, Solbiati L, et al. Complications of microwave ablation for liver tumors: results of a multicenter study. Cardiovasc Intervent Radiol. 2012;35(4):868–874. doi:10.1007/s00270-011-0241-8.

[15] Poggi G, Montagna B, DI Cesare P, et al. Microwave ablation of hepatocellular carcinoma using a new percutaneous device: preliminary results. Anticancer Res. 2013;33:1221–1227.

[16] Horn JC, Patel RS, Kim E, et al. Percutaneous microwave ablation of renal tumors using a gas-cooled 2.4-GHz probe: technique and initial results. J Vasc Interv Radiol. 2014;25(3):448–453. doi:10.1016/j.jvir.2013.10.029.

[17] Ziemlewicz TJ, Hinshaw JL, Lubner MG, et al. Percutaneous microwave ablation of hepatocellular carcinoma with a gas-cooled system: initial clinical results with 107 tumors. J Vasc Interv Radiol. 2015;26(1):62–68. doi:10.1016/j.jvir.2014.09.012.

[18] Ryan TP, Brace CL. Interstitial microwave treatment for cancer: historical basis and current techniques in antenna design and performance. Int J Hyperthermia. 2017;33(1):3–14. doi:10.1080/02656736.2016.1214884.

[19] Pfannenstiel A, Iannuccilli J, Cornelis FH, et al. Shaping the future of microwave tumor ablation: a new direction in precision and control of device performance. Int J Hyperthermia. 2022;39(1):664–674. doi:10.1080/02656736.2021.1991012.

[20] European association for the study of the liver, european organisation for research and treatment of cancer. EASL-EORTC Clinical Practice Guidelines: management of Hepatocellular Carcinoma. J Hepatol. 2012;56:908–943.

[21] Wright AS, Lee FT, Mahvi DM. Hepatic microwave ablation with multiple antennae results in synergistically larger zones of coagulation necrosis. Ann Surg Oncol. 2003;10(3):275–283. doi:10.1245/aso.2003.03.045.

[22] Mukherjee S, Curto S, Albin N, et al. Multiple-antenna microwave ablation: analysis of non-parallel antenna implants. International Society for Optics and Photonics; 2015 cited 2018 Jan 17]. p. 93260U. Available from: https://www.spiedigitallibrary.org/conference-proceedings-of-spie/9326/93260U/Multiple-antenna-microwave-ablation–analysis-of-non-parallel-antenna/10.1117/12.2080349.short. doi:10.1117/12.2080349.

[23] Simo KA, Tsirline VB, Sindram D, et al. Microwave ablation using 915-MHz and 2.45-GHz systems: what are the differences? HPB (Oxford). 2013;15(12):991–996. doi:10.1111/hpb.12081.

[24] Laimer G, Schullian P, Bale R. Stereotactic thermal ablation of liver tumors: 3D planning, multiple needle approach, and intraprocedural image fusion are the key to Success-A narrative review. Biology (Basel). 2021;10(7):644. doi:10.3390/biology10070644.

[25] Goldberg SN. Can the injection of adjuvant gels accelerate heating for more robust thermal ablation of tumors? Radiology. 2019;291(2):511–512. doi:10.1148/radiol.2019190074.

[26] Paulet E, Aubé C, Pessaux P, et al. Factors limiting complete tumor ablation by radiofrequency ablation. Cardiovasc Intervent Radiol. 2008;31(1):107–115. doi:10.1007/s00270-007-9208-1.

[27] Atwell TD, Carter RE, Schmit GD, et al. Complications following 573 percutaneous renal radiofrequency and cryoablation procedures. J Vasc Interv Radiol. 2012;23(1):48–54. doi:10.1016/j.jvir.2011.09.008.

[28] Gillams AR, Lees WR. CT mapping of the distribution of saline during radiofrequency ablation with perfusion electrodes. Cardiovasc Intervent Radiol. 2005;28(4):476–480. doi:10.1007/s00270-004-0284-1.

[29] Park WKC, Maxwell AWP, Frank VE, et al. Evaluation of a novel thermal accelerant for augmentation of microwave energy during

image-guided tumor ablation. Theranostics. 2017;7(4):1026–1035. doi:10.7150/thno.18191.
[30] Park WKC, Maxwell AWP, Frank VE, et al. The in vivo performance of a novel thermal accelerant agent used for augmentation of microwave energy delivery within biologic tissues during image-guided thermal ablation: a porcine study. Int J Hyperthermia. 2018;34(1):11–18. doi:10.1080/02656736.2017.1317367.
[31] Wang S, Zhang N, Hu T, et al. Viscosity-Lowering effect of amino acids and salts on highly concentrated solutions of two IgG1 monoclonal antibodies. Mol Pharm. 2015;12(12):4478–4487. doi:10.1021/acs.molpharmaceut.5b00643.
[32] Park WKC, Dupuy DE, Walsh EG. Thermal accelerant compositions and methods of use [Internet]. 2020 [cited 2023 Feb 21]. Available from: https://patents.google.com/patent/US10722289B2/en.
[33] Maxwell AWP, Park WKC, Baird GL, et al. Effects of a thermal accelerant gel on microwave ablation zone volumes in lung: a porcine study. Radiology. 2019;291(2):504–510. doi:10.1148/radiol.2019181652.
[34] Maxwell AWP, Park WKC, Baird GL, et al. Adjuvant thermal accelerant gel use increases microwave ablation zone temperature in porcine liver as measured by MR thermometry. J Vasc Interv Radiol. 2020;31(8):1357–1364. doi:10.1016/j.jvir.2020.01.010.
[35] Cavagnaro M, Amabile C, Bernardi P, et al. A minimally invasive antenna for microwave ablation therapies: design, performances, and experimental assessment. IEEE Trans Biomed Eng. 2011;58(4):949–959. doi:10.1109/TBME.2010.2099657.
[36] Mohtashami Y, Hagness SC, Behdad N. A hybrid slot/monopole antenna with directional heating patterns for microwave ablation. IEEE Trans. Antennas Propagat. 2017;65(8):3889–3896. doi:10.1109/TAP.2017.2714020.
[37] Yang D, Bertram JM, Converse MC, et al. A floating sleeve antenna yields localized hepatic microwave ablation. IEEE Trans Biomed Eng. 2006;53(3):533–537. doi:10.1109/TBME.2005.869794.
[38] Brace CL, Laeseke PF, van der Weide DW, et al. Microwave ablation with a triaxial antenna: results in ex vivo bovine liver. IEEE Trans Microw Theory Tech. 2005;53(1):215–220. doi:10.1109/TMTT.2004.839308.
[39] Etoz S, Brace CL. Analysis of microwave ablation antenna optimization techniques. Int J RF Microw Comput Aided Eng. 2018;28(3):e21224. doi:10.1002/mmce.21224.
[40] Sawicki JF, Shea JD, Behdad N, et al. The impact of frequency on the performance of microwave ablation. Int J Hyperth Off J Eur Soc Hyperthermic Oncol North Am Hyperth Group. 2016;1–8.
[41] Bottiglieri A, Ruvio G, O'Halloran M, et al. Exploiting tissue dielectric properties to shape microwave thermal ablation zones. Sensors. 2020;20(14):3960. doi:10.3390/s20143960.
[42] Deshazer G, Merck D, Hagmann M, et al. Physical modeling of microwave ablation zone clinical margin variance. Med Phys. 2016;43(4):1764–1776. doi:10.1118/1.4942980.
[43] Cavagnaro M, Pinto R, Lopresto V. Numerical models to evaluate the temperature increase induced by ex vivo microwave thermal ablation. Phys Med Biol. 2015;60(8):3287–3311. doi:10.1088/0031-9155/60/8/3287.
[44] Sebek J, Taeprasartsit P, Wibowo H, et al. Microwave ablation of lung tumors: a probabilistic approach for simulation-based treatment planning. Med Phys. 2021;48(7):3991–4003. doi:10.1002/mp.14923.
[45] Ji Z, Brace CL. Expanded modeling of temperature-dependent dielectric properties for microwave thermal ablation. Phys Med Biol. 2011;56(16):5249–5264. doi:10.1088/0031-9155/56/16/011.
[46] Lopresto V, Pinto R, Lovisolo GA, et al. Changes in the dielectric properties of ex vivo bovine liver during microwave thermal ablation at 2.45 GHz. Phys Med Biol. 2012;57(8):2309–2327. doi:10.1088/0031-9155/57/8/2309.
[47] Bhattacharya A, Mahajan RL. Temperature dependence of thermal conductivity of biological tissues. Physiol Meas. 2003;24(3):769–783. doi:10.1088/0967-3334/24/3/312.
[48] Lopresto V, Argentieri A, Pinto R, et al. Temperature dependence of thermal properties of ex vivo liver tissue up to ablative temperatures. Phys Med Biol. 2019;64(10):105016. doi:10.1088/1361-6560/ab1663.
[49] Fallahi H, Sebek J, Prakash P. Broadband dielectric properties of ex vivo bovine liver tissue characterized at ablative temperatures. IEEE Trans Biomed Eng. 2021;68(1):90–98. doi:10.1109/TBME.2020.2996825.
[50] Faridi P, Keselman P, Fallahi H, et al. Experimental assessment of microwave ablation computational modeling with MR thermometry. Med Phys. 2020;47(9):3777–3788. doi:10.1002/mp.14318.
[51] Deshazer G, Hagmann M, Merck D, et al. Computational modeling of 915 MHz microwave ablation: comparative assessment of temperature-dependent tissue dielectric models. Med Phys. 2017;44(9):4859–4868. doi:10.1002/mp.12359.
[52] IT'IS Foundation. Tissue Properties Database V4.1 [Internet]. IT'IS Foundation; 2022 [cited 2023 May 8]. Available from: https://itis.swiss/virtual-population/tissue-properties/downloads/database-v4-1/.
[53] Hall SK, Ooi EH, Payne SJ. Cell death, perfusion and electrical parameters are critical in models of hepatic radiofrequency ablation. Int J Hyperthermia. 2015;31(5):538–550. doi:10.3109/02656736.2015.1032370.
[54] Shrivastava D, Vaughan JT. A generic bioheat transfer thermal model for a perfused tissue. J Biomech Eng. 2009;131(7):074506.
[55] Pearce JA. Models for thermal damage in tissues: processes and applications. Crit Rev Biomed Eng. 2010;38(1):1–20. doi:10.1615/critrevbiomedeng.v38.i1.20.
[56] Haemmerich D. 1 - Mathematical modeling of heat transfer in biological tissues (bioheat transfer). In: Prakash P, Srimathveeravalli G, editors. Principles and technologies for electromagnetic energy based therapies. Academic Press; 2022. p. 1–24. doi:10.1016/B978-0-12-820594-5.00012-5.

Appendix

To verify the local heating enhancement in HeatSYNC™ gel, as anticipated by the dielectric property measurements, we conducted an experiment designed to measure the temperature within the HeatSYNC gel, in addition to regions adjacent to the gel. To facilitate this, we filled a polyimide tube (3 mm diameter) with either agar (for control) or the HeatSYNC gel and placed the polyimide tube between fiber optic sensor channels 1 and 4 on one side of applicator as shown in Figure A1. Spacing between sensors and applicator agree with all other *ex vivo* experiments in liver. The agarose mixture consists of 74.75% deionized water, 23% sugar, 0.25% salt, and 2% agar. To prepare the phantom, we heated deionized water poured in beaker with hot plate and magnetic stirrer. Once temperature reached 50 °C, we added all other ingredients and continued heating until temperature reached 85 °C while continuously mixing. After reaching 85 °C, the hot plate was turned off and the mixture was left to cool down. Before solidification of mixture, we poured respective amounts of the phantom into the fixture templates and one polyimide tube for experiments. The measured dielectric (at 2.45 GHz) and thermal properties of agar are specifically relative permittivity $\sim 61 \pm 2$, effective conductivity $\sim 2.45 \pm 0.05$ S/m, volumetric heat capacity $\sim 3.5 \pm 0.2$ MJ/kg/K, and thermal conductivity $\sim 0.5 \pm 0.06$ W/m/K.

From the measured temperature data, transient temperatures at each sensor were compared between control, when agar was present in polyimide tube, and the test experiment with HeatSYNC™ gel present in polyimide tube. Figure A2 shows transient temperature rise at the four fiber optic temperature sensor locations. As anticipated by the higher electrical conductivity of the HeatSYNC gel compared to the phantom (and given that the electrical conductivity of the HeatSYNC gel increases with temperature), we observed greater rate of heating and maximum temperature at channel 3 when the polyimide tube was filled with the HeatSYNC gel compared to agar (i.e., control). It was also observed that the temperature measured at channel 1, in between the polyimide tube and the ablation applicator, was higher for the experiment with the HeatSYNC gel compared to control, which

could be attributed to the thermal gradient established by the hotspot within the polyimide tube filled with HeatSYNC. There were no substantive differences in temperatures observed at Channel 2 and 4. These data support the anticipated greater absorption in the HeatSYNC gel compared to control based on dielectric properties, and suggest that overall extent of ablation zone due to the HeatSYNC gel is limited in situations where the gel position is tightly constrained (e.g., as in the polyimide tube).

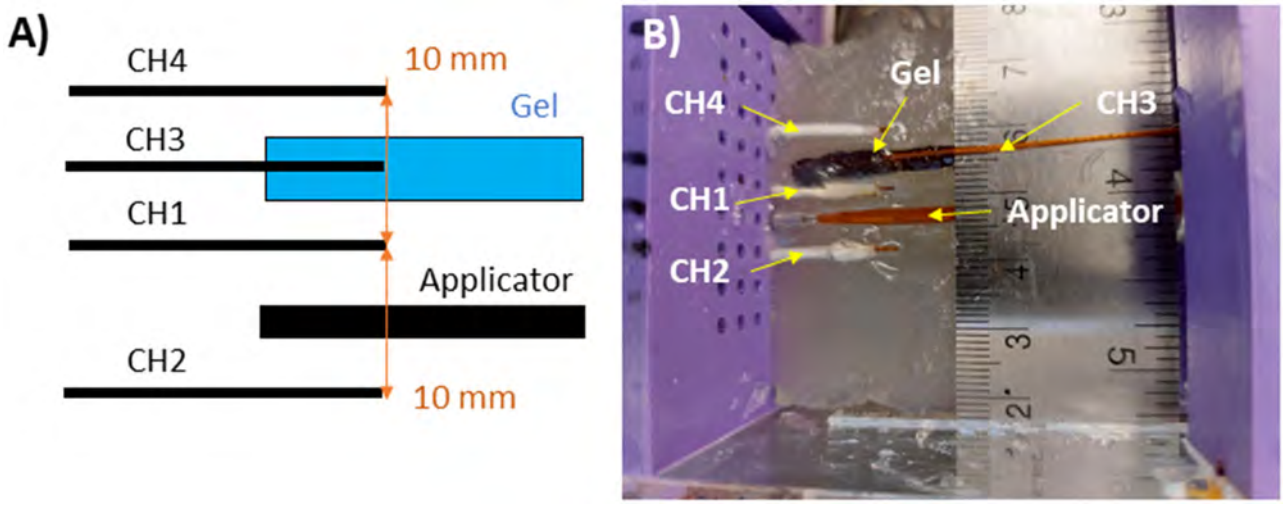

Figure A1. MWA applicator and fiber Optics positioning around polyimide tube with either agar or HeatSYNC™. Figure A) shows schematic, and figure B) shows example of probe spacing measurement.

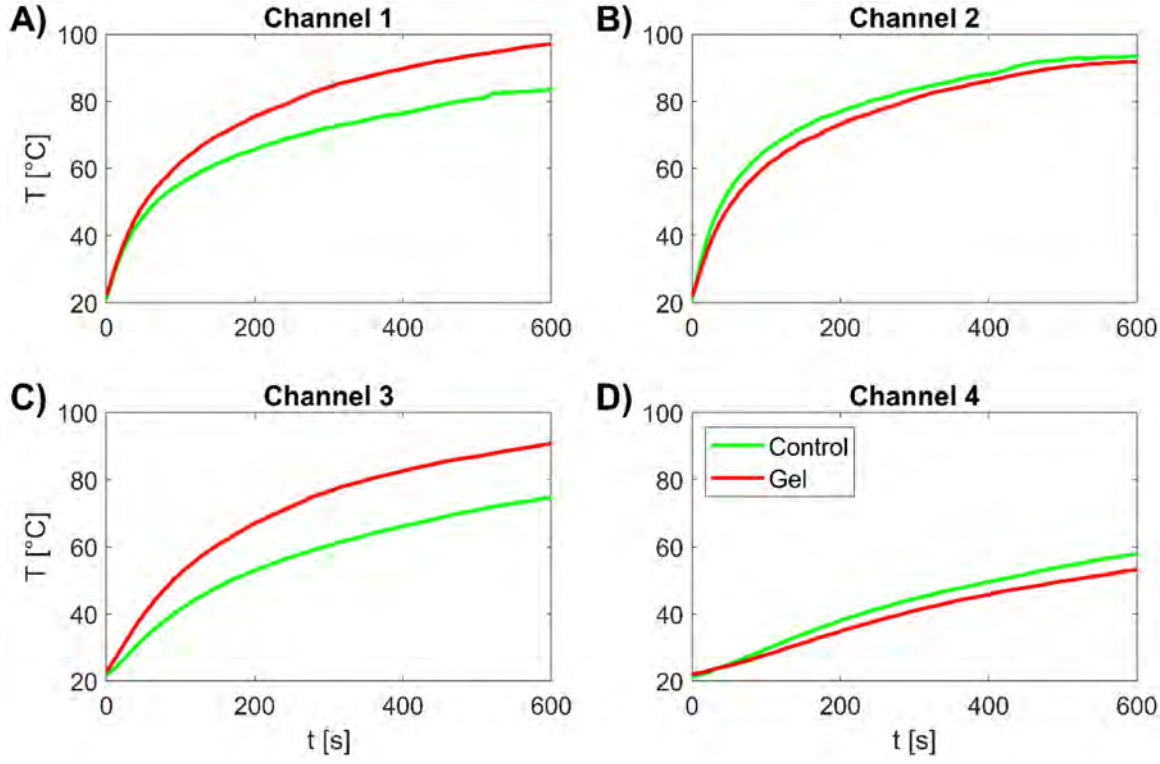

Figure A2. Temperatures as measured at the four fiber optic locations illustrated in Figure A1. Channel 1 (A) depicts temperature between gel and applicator, 5 mm away from applicator axis. Channel 2 (B) stands for temperature measured at opposite side of applicator also 5 mm away from applicator axis. Channel 3 (C) depicts temperatures measured inside polyimide tube with either thermal accelerant (gel) or agar (control). Channel 4 (D) shows temperatures measured on the other side of gel away from applicator.